

The mechanism of force transmission at bacterial focal adhesion complexes

Laura M. Faure^{1*}, Jean-Bernard Fiche^{2*}, Leon Espinosa^{1*}, Adrien Ducret^{1,3}, Vivek Anantharaman⁴, Jennifer Luciano¹, Sébastien Lhospice¹, Salim T. Islam¹, Julie Tréguier¹, Mélanie Sotes¹, Erkin Kuru⁵, Michael S. Van Nieuwenhze⁶, Yves V. Brun³, Olivier Théodoly⁷, L. Aravind⁴, Marcelo Nollmann² & Tâm Mignot¹

Various rod-shaped bacteria mysteriously glide on surfaces in the absence of appendages such as flagella or pili. In the *delta-proteobacterium Myxococcus xanthus*, a putative gliding motility machinery (the Agl–Glt complex) localizes to so-called focal adhesion sites (FASs) that form stationary contact points with the underlying surface. Here we show that the Agl–Glt machinery contains an inner-membrane motor complex that moves intracellularly along a right-handed helical path; when the machinery becomes stationary at FASs, the motor complex powers a left-handed rotation of the cell around its long axis. At FASs, force transmission requires cyclic interactions between the molecular motor and the adhesion proteins of the outer membrane via a periplasmic interaction platform, which presumably involves contractile activity of motor components and possible interactions with peptidoglycan. Our results provide a molecular model of bacterial gliding motility.

Certain rod-shape bacteria move along their long axes in the absence of extracellular appendages such as flagella or pili, in a process called gliding motility¹. In *Myxococcus xanthus*, gliding is mediated by bacterial FASs. During gliding motility, FASs assemble at the leading cell pole and retain a fixed position relative to the surface until they disassemble at the lagging cell pole¹. FASs contain a molecular machinery, the Agl–Glt (adventurous gliding and gliding transducer) complex, which comprises more than fourteen proteins^{2–4}. Genetic analysis has suggested that this machinery is formed by two membrane-associated systems: (i) a putative three-protein TolQR-like proton motive force (PMF)-driven channel comprising AglR, AglQ and AglS (the suspected energy-producing system)^{3,5,6}; and (ii) a putative eleven-protein integral envelope-associated complex (containing GltA–K) that interacts with the Agl system^{2–4}. These machineries are further connected to a cytosolic protein complex formed by the AglZ protein, the Ras-like G-protein MgIA and the MreB actin cytoskeleton (hereafter called the MreB complex⁷; Fig. 1a). This MreB complex recruits, and promotes the assembly of the Agl–Glt complex (Fig. 1a). Directional movements of the Agl–Glt complex from the leading towards the lagging cell pole have been suggested to propel the cell forward^{3,8}, but how these movements may be transduced into cell movement remains unknown^{5,9}. Here, we reveal the functional architecture of the Agl–Glt complex and establish how its activity is transduced to the contact surface across the highly structured layers of the cell envelope.

Intracellular helically moving engines drive propulsion

We quantitatively characterized the dynamic behaviour of FASs by analysing the motions of AglZ–YFP (yellow fluorescent protein)-containing complexes using total internal reflection fluorescence microscopy (TIRFM). Cells attached to a chitosan-coated surface alternated between motile and non-motile states. In these conditions, we were able to capture the movement of AglZ–YFP clusters over extended

periods of time with high temporal resolution. Two main AglZ–YFP cluster populations were observed: static and dynamic (Fig. 1b; blue and orange, respectively). Motile cells on chitosan exhibited at least one static AglZ–YFP cluster, indicating that a single static cluster is necessary and sufficient for cell propulsion. We also observed dynamic AglZ–YFP clusters. These clusters tended to form at one cell pole and migrate directionally towards the opposite pole (Fig. 1b and Extended Data Fig. 1a). On average, clusters formed every minute and moved at a constant velocity ($3.2 \pm 0.9 \mu\text{m min}^{-1}$, $n = 227$) over distances of $1.5 \pm 1 \mu\text{m}$ ($n = 203$), often becoming dissociated upon reaching the opposite pole. Cluster speeds varied within and between cells (Extended Data Fig. 1b), possibly because of variations in the number of motor units in a cluster (see below) and changes in PMF levels between cells^{3,6}. Dynamic clusters are likely to represent unattached motility complexes because: (i) in motile cells, they were detected only if a fixed cluster was also present; and (ii) in most cells the transition from a non-motile to a motile state coincided with cluster immobilization (>85%, $n = 34$; Fig. 1b, orange–blue cluster). To characterize this behaviour quantitatively, we measured the correlation (β) between cell movement and the presence of static and dynamic clusters (Fig. 1b, lower panel). Importantly, the presence of static, but not dynamic, clusters was highly correlated with cell movement (Fig. 1c, $n = 95$).

Close examination of dynamic clusters by TIRF revealed that they not only move between poles but also move across the cell width following a helical path (Fig. 1d). The helicity, characterized by the angle of a helix projected on a plane (φ_a , Fig. 1e), was constant between cells ($\varphi_a = 78^\circ \pm 5^\circ$, $n = 54$; Fig. 1e). In most cases (92%, $n = 54$), the direction of rotation of AglZ–YFP clusters was counterclockwise relative to the direction of movement, denoting a right-handed helical path. Treating the cells with A22, a drug that inhibits MreB polymerization¹⁰, decreased the number of dynamic clusters per cell (Extended Data Fig. 1c, d) but, notably, not their helical movement or directionality (Extended Data Fig. 1e).

¹Laboratoire de Chimie Bactérienne, CNRS-Aix Marseille University UMR7283, Institut de Microbiologie de la Méditerranée, 13009 Marseille, France. ²Centre de Biochimie Structurale, CNRS UMR5048, INSERM U1054, Montpellier University, 29 rue de Navacelles, 34090 Montpellier, France. ³Department of Biology, Indiana University, Bloomington, Indiana 47405, USA. ⁴National Center for Biotechnology Information, National Library of Medicine, National Institutes of Health, Bethesda, Maryland 20892, USA. ⁵Interdisciplinary Biochemistry Program, Indiana University, Bloomington, Indiana 47405, USA. ⁶Department of Chemistry, Indiana University, Bloomington, Indiana 47405, USA. ⁷Adhesion and Inflammation laboratory, INSERM U1067, Aix Marseille University UMR7333, 13288 Marseille, France.

*These authors contributed equally to this work.

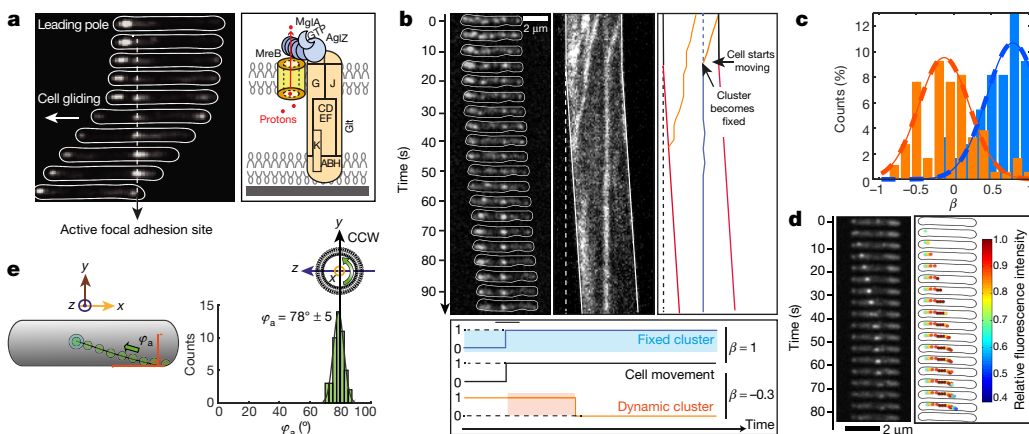


Figure 1 | The *Myxococcus* motility complex moves directionally along a helical path. **a**, Spatial regulation of the *Myxococcus* motility complex. A motile AglZ-YFP-expressing cell showing a complete assembly cycle is shown at 30-s intervals. A current view of an Agl (blue)–Glt (yellow) complex at an FAS is shown^{2,7,19}. Assembly occurs at the leading cell pole following interactions between MgI_A-GTP, MreB and AglZ (right panel, blue)⁸. The position of the Glt proteins is drawn based on published works^{2–5,7,20}. **b**, Immobilization of AglZ-YFP clusters correlates with cell movement. TIRFM of AglZ-YFP in a cell that shifts to motility on a chitosan-treated surface. Images were acquired every 0.5 s. Selected time frames and the corresponding high-resolution kymograph are shown. Two dynamic (orange) clusters are shown. Note that cell movement (indicated by the dashed line showing the initial cell position) is observed

only when a cluster becomes stationary (see orange-blue cluster). Scale bar, 2 μ m. Lower panel: calculation of the correlation coefficient (R) between the presence of a cluster and cell movement. The fixed cluster (blue) is highly correlated with cell movement ($\beta = 1$), while the dynamic cluster (orange) is partially anti-correlated ($\beta = -0.3$). **c**, Distribution of R for fixed (blue) and dynamic clusters (orange), $n = 95$ (six biological replicates). **d**, AglZ-YFP clusters move along helical trajectories. TIRFM at selected time frames of a dynamic AglZ-YFP cluster in a non-motile cell are shown. Scale bar, 2 μ m. **e**, Measurement of the trajectory angle (φ_a) from $n = 54$ (eight biological replicates) single trajectories of dynamic AglZ-YFP clusters (top panels). Histogram of φ_a and Gaussian fit (grey line) are shown. The mean angle is shown with a dashed vertical line and corresponds to counterclockwise trajectories.

Moving cells rotate in a clockwise direction

We reasoned that if propulsion was linked to the counterclockwise trafficking of AglZ-YFP-containing motility complexes, then a gliding cell body should rotate along a similar helical path but of opposite handedness (that is, clockwise; Fig. 2a). To test this idea, we followed the dynamics of fiducial markers (artificial fluorescent D-amino acids, or TADA) fixed to the cell periphery during cell movement (Extended Data Fig. 2a–d). In motile cells, TADA clusters moved from one side

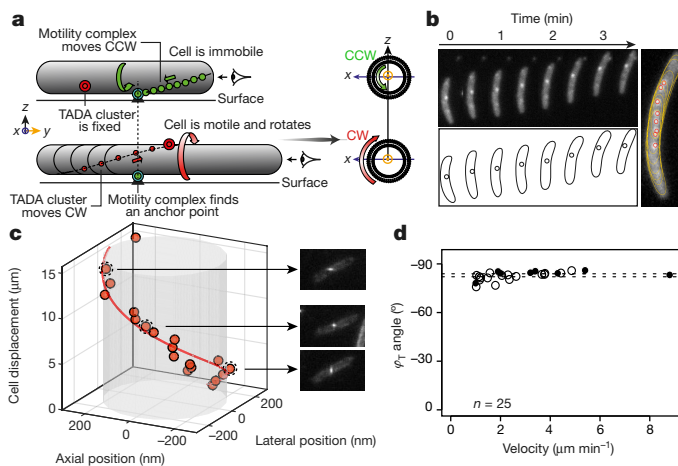


Figure 2 | *Myxococcus* cells rotate during motility. **a**, The helical movement of intracellular motors predicts rotation of the cell during movement. **b**, Rotation of a TADA-bright cluster in a motile cell (30-s intervals) and in a sum-type projection (right). The cartoon representation shows the position of the centroid of the cluster relative to the cell outline. **c**, Three-dimensional positions of a TADA-bright cluster measured by astigmatism (orange dots) illustrating the clockwise rotation of the motile cell ($n = 8$; five biological replicates). Snapshots of the cell are displayed, illustrating the deformation of the microscope point spread function as a function of the axial position. **d**, Rotation angle of TADA-bright clusters (φ_T) as a function of cell velocity from astigmatism (filled circles, $83.9^\circ \pm 2.5^\circ$; $n = 8$, 5 biological replicates) and intensity variations (open circles $82.0^\circ \pm 2.6^\circ$; $n = 17$, three technical replicates).

of the cell to the opposite side with angular velocities proportional to the speed of motility (Fig. 2b and Extended Data Fig. 2e), consistent with TADA clusters reporting on the overall rigid-body rotational movement of the cell during propulsion.

To determine the direction of rotation, we directly tracked the 3D positions of TADA clusters during cell movement by inducing astigmatism into the optical detection path¹¹ (see Methods). In agreement with our predictions, TADA clusters rotated in the clockwise direction during cell propulsion (Fig. 2c and Extended Data Fig. 2f; $n = 8$). These observations were confirmed by monitoring the changes in fluorescence intensity produced when TADA clusters moved in and out of the imaging plane during cell movement (see Methods and Extended Data Fig. 2g; $n = 17$). The rotation angle for TADA clusters (φ_T) was constant between cells ($82.6^\circ \pm 2.7^\circ$, $n = 25$, as measured by both methods; Fig. 2d) and closely matched the angle of rotation (φ_a) measured for AglZ-YFP clusters ($78^\circ \pm 5^\circ$). Interestingly, φ_T did not vary significantly with cell speed (Fig. 2d). Together, these findings indicate that anchoring of dynamic AglZ-YFP-containing complexes leads to the clockwise rotation and forward propulsion of the cell.

Functional analysis of the Agl-Glt motility complex

To gain further insight into the molecular mechanism of motility, we genetically dissected the functional groups composing the Agl-Glt machinery (Fig. 1a). Notably, mutations in *agl* and *glt* genes led to aberrant localization patterns and perturbation of AglZ-YFP cluster dynamics (Fig. 3a and Extended Data Fig. 3a). The global effect of each mutation on the localization pattern of AglZ-YFP was evaluated by measuring four observables: the proportion of cells with AglZ-YFP clusters, the mean number of clusters, and the longitudinal and radial distributions of clusters for wild-type and mutant cells (Fig. 3a and Extended Data Fig. 3b). Principal component analysis (PCA) was used to quantitatively characterize the effect of each mutant in the assembly of AglZ-YFP clusters (see Methods). This statistical method allowed us to convert the set of correlated observables into a set of linearly uncorrelated principal components (PCs).

The first three principal components described >87% of the variance (Extended Data Fig. 4a–d). PC1 represented a linear combination of

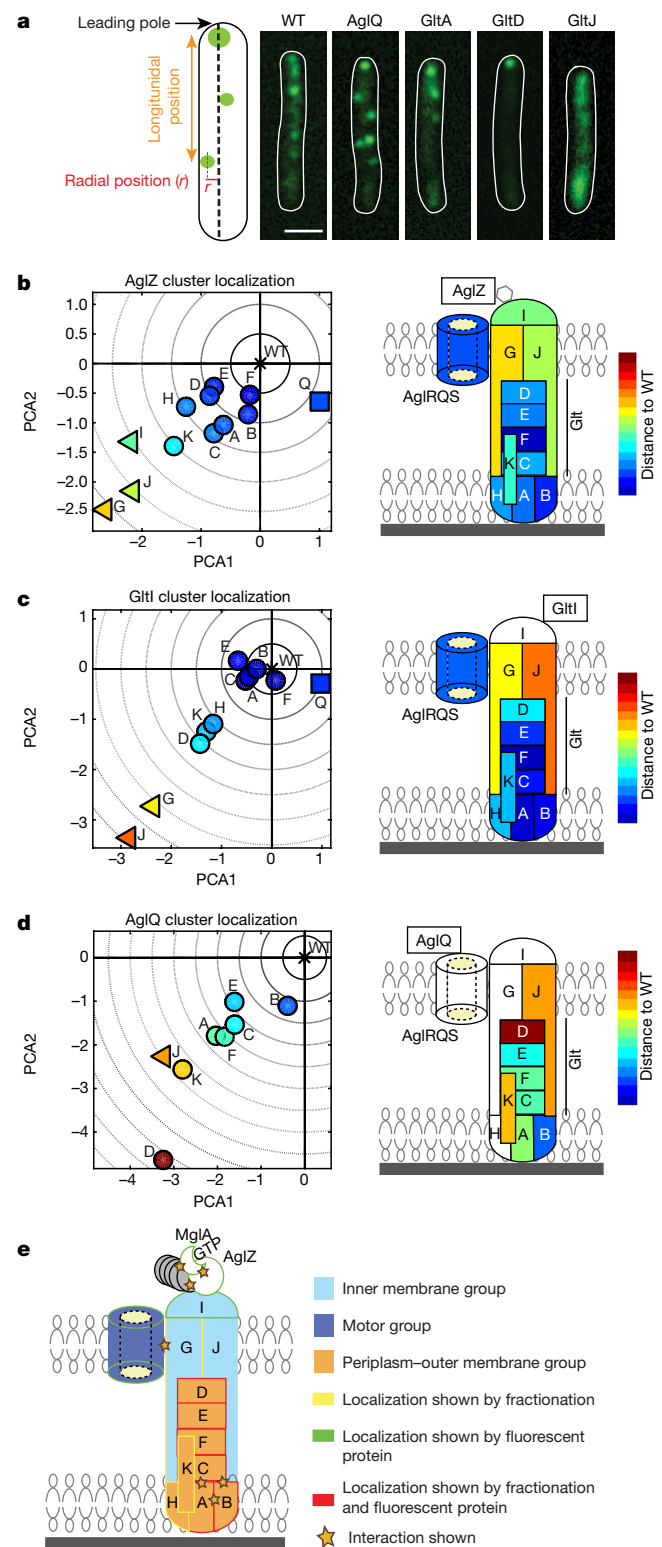


Figure 3 | Functional architecture of the Agl-Glt machinery. **a**, The localization of AglZ-YFP is affected to different extents in *agl-glt* mutants. The number and position (longitudinal and radial) of clusters was determined in each mutant background and their effect analysed by PCA (see Methods). Scale bar, 1 μ m. **b–d**, The effect of mutations in assembly dynamics of AglZ-YFP, GltI-YFP and AglQ-mCherry plotted in PC coordinates. Triangles represent inner membrane (IM) group proteins, squares represent motor components and circles represent other components (periplasm-outer membrane (OM)). Right panels show schematic representations of the projections of the defined gene groups with respect to their predicted/shown localization from^{2–5,7,20}. Colour code represents distance to the wild type (WT) in PC space. Letters represent each protein subunit of the Agl-Glt complex. **e**, The compilation of PCA (**b–d**) superimposed to available data^{2–5,7,20} suggests that the motility machinery consists of a molecular motor (dark blue), an inner membrane-cytosolic group (light blue) and a large periplasm-outer membrane group (orange).

the origin and the direction represent the relative effect of a mutation on the number and distribution of AglZ-YFP clusters. Mutations in predicted inner membrane components (GltI, G, J) produced the largest perturbations in the assembly dynamics of AglZ-YFP clusters, whereas mutations in periplasmic outer-membrane group proteins (GltA, C, D, E, H, K) displayed the lowest effect (Fig. 3b). Interestingly, mutations in AglQ (motor) affected AglZ-YFP cluster formation in a qualitatively different manner, represented by a direction in PC space orthogonal to that observed for other mutants.

We refined the functional connections between *agl* and *glt* genes by further investigating the effect of gene deletions on the formation of GltI-YFP⁷ and AglQ-mCherry^{3,7} clusters (GltI and AglQ are putative cytosolic and motor components of the gliding machine, respectively). The overall effects of gene deletions on the number and distribution of GltI-YFP clusters were similar to those observed for AglZ-YFP clusters, consistent with GltI and AglZ belonging to the same functional group (Fig. 3c). Mutations in GltI had a large effect on GltI-YFP assembly (Fig. 3c). Interestingly, mutations in GltD, GltH and GltK had a larger effect than did mutations in other proteins in their subgroup (for example, GltA, B, C, E), suggesting that direct protein-protein interactions between these proteins and factors of the GltI subgroup may be needed for GltI-YFP localization (Fig. 3c). Finally, we analysed the effect of deletions in the assembly of motor components (AglQ). Strikingly, deletion of factors in all subgroups led to severe perturbations in the formation of AglQ-mCherry fluorescent clusters (Fig. 3d), suggesting that the motor may require several contacts with different Glt proteins to form functional clusters. However, specific components exhibited differential roles: deletion of GltJ, GltD and GltK had the largest effects, whereas deletion of GltB barely affected the formation of AglQ-mCherry clusters (Fig. 3d). Overall, these data indicate that the motility complex is divided into several distinct functional groups (Fig. 3e).

Motor docks to OM complex during propulsion

To determine the sequence of events leading to the assembly of propulsive complexes, we imaged the dynamic localization of AglZ-YFP (cytosolic-inner membrane group) simultaneously with that of proteins belonging to each of the other functional subgroups: AglQ (motor), GltD (periplasmic), or GltC-mCherry (periplasm-outer membrane complex) (Fig. 4a, c, e). Under conventional epifluorescence microscopy, cytosolic (AglZ) and motor components (AglQ) in motile cells (on 1.5% agar) displayed a strong ability to form clusters, in contrast to the dispersed localization of periplasmic and outer membrane complex components (GltC, D) to the cell periphery (Extended Data Fig. 5a). Thus, we used TIRFM to image the dynamic localization of these factors in motile cells adhered to chitosan-coated glass. AglQ-mCherry and AglZ-YFP co-localized in both stationary and mobile clusters, indicating that these proteins form a stable

the number of AglZ-YFP clusters, longitudinal cluster position, and proportion of cells with clusters. PC2 mostly represented the average number of clusters detected per cell, while PC3 was essentially dominated by the mean radial cluster position (Extended Data Fig. 4a–d). A synthetic representation of results can be obtained by plotting the mean position of each mutant in a principal component space where the wild type is arbitrarily positioned at the origin (Fig. 3b; for clarity only PC1 and PC2 are shown but the analysis is computed from PC1–3; Extended Data Fig. 4e). Therefore, for each mutant, the distance to

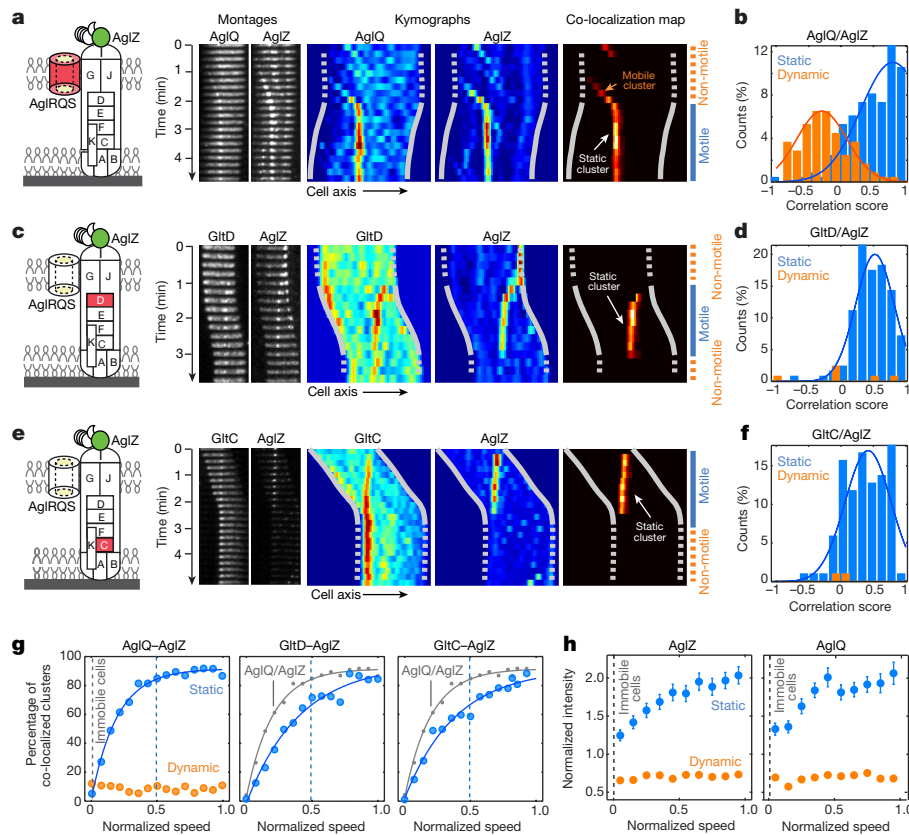


Figure 4 | Dynamic interactions between the intracellular and outer membrane complexes generate propulsion. **a**, Simultaneous dynamics of AglZ-YFP and AglQ-mCherry and correlation to the motility phases. TIRFM time-lapse images and corresponding kymographs are shown for individual fluorescent fusions and in a heat map showing the computed co-localization scores. **b**, AglZ and AglQ co-localize in the inner membrane trafficking complex ($n = 156$ cells; two biological replicates). Correlation scores reflect the correlation between cell movement and static co-localized clusters. **c**, **d**, Simultaneous dynamics of AglZ-YFP and GltD-mCherry and correlation to the motility phase ($n = 121$ cells; seven biological replicates). Legend as in **a**, **b**. **e**, **f**, Simultaneous dynamics of AglZ-YFP and GltC-mCherry and correlation to the motility phase

($n = 100$ cells; three biological replicates). Legend as in **a**, **b**, **g**, Correlation between cell velocity and number of active complexes. For a given value of the cell speed (V), the percentage of co-localized clusters represents the proportion of events in which a cell was moving at speed V and an active cluster containing both AglZ and AglQ, GltD or GltC was detected. The percentage of co-localization is shown as a function of normalized cell speed (where 1 is the maximum cell speed). **h**, Correlation between cell velocity and intensity of AglZ and AglQ clusters. Intensity was normalized with respect to the average intensity measured for dynamic clusters and shown as a function of normalized cell speed. Error bars represent s.e.m. calculated according to the total number of cells analysed ($n = 114$ cells for AglZ, $n = 100$ for AglQ).

complex in the bacterial inner membrane (Fig. 4a; see also Methods and Extended Data Figs 5b, c, 6). To investigate whether clusters containing both AglZ and AglQ were linked to cell motility, we calculated for each cell the correlation between cell movement and co-localization and computed the distributions for both stationary and mobile clusters (Fig. 4b; see also Methods and Extended Data Fig. 7). The presence of stationary clusters was highly correlated to cell movement, whereas that of mobile clusters was not, consistent with AglZ and AglQ being part of the trafficking internal complex (Fig. 4b). By contrast, GltD-mCherry and GltC-mCherry co-localized with AglZ-YFP only in stationary clusters (Fig. 4c, e and Extended Data Fig. 5b, c) and co-localization of stationary AglZ-GltC/D clusters was highly correlated to cell movement (Fig. 4d, f). These data strongly suggest that cytosolic–inner membrane and motor complexes assemble together in a mobile unit that requires a physical connection to periplasmic and outer membrane components to form stationary clusters that impart cell movement.

To investigate this hypothesis further, we determined the correlation between cell speed and the proportion of clusters containing both AglZ and AglQ, GltC or GltD (Fig. 4g). Dynamic clusters containing AglZ and AglQ were observed in motile cells, but their number was independent of cell speed, indicating that they are not propulsive by themselves (Fig. 4g). On the contrary, the proportion of AglZ-AglQ clusters that were stationary increased rapidly with cell speed (Fig. 4g). The number of AglZ-AglQ clusters reached a maximum at $\sim 50\%$ of

the cell maximum speed ($V_{1/2}$), suggesting that this number is not a limiting factor (Fig. 4g). In fact, the recruitment of GltD and GltC to FASs could be a limiting step because a substantial number of static AglZ clusters lack GltD and, especially, GltC (Extended Data Fig. 5b, c). Consistent with this finding, the number of stationary AglZ-GltD and AglZ-GltC clusters was only $\sim 60\%$ of the maximum at $V_{1/2}$ and full speed was reached only when the percentage of GltD-GltC stationary clusters recruited to FASs saturated (Fig. 4g). Thus, the recruitment of GltD and GltC to FASs is required for propulsion, probably because these proteins belong to complexes that link the motor to the external surface.

To test further whether the stoichiometry of Agl–Glt components regulates the activity of FASs, we measured how the mean fluorescence intensity of stationary and mobile clusters changed with normalized cell speed (Fig. 4h and see Methods). Cell speed increased with the number of AglZ and AglQ subunits accumulating in stationary clusters (Fig. 4h). By contrast, the proportion of these subunits in mobile clusters was systematically lower and uncorrelated with cell speed (Fig. 4h). All in all, these results show that stationary focal adhesion complexes form as a result of the transient recruitment of periplasmic and outer membrane proteins by the mobile PMF-driven inner membrane complex. Importantly, the activity of stationary complexes is regulated at two levels: by the number of Agl motor units (force generation) and by the number of local contacts with periplasmic–outer membrane components (transmission).

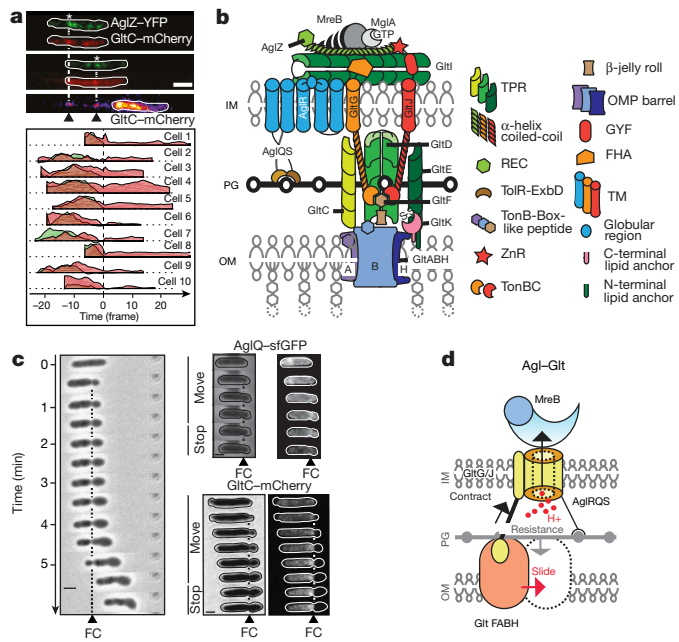


Figure 5 | Cyclic contacts between the inner membrane motor and outer membrane adhesins drive propulsion. **a**, GltC-mCherry is released by gliding cells at focal adhesion complexes. Top, TIRFM snapshots for a representative cell expressing both GltC-mCherry (red) and AglZ-YFP (green). The positions of the GltC clusters on the surface coincide with the positions of focal adhesion complexes (white asterisk). Time frames, 15 s. Scale bar, 2 μ m. Bottom, variation in intensity of GltC-mcherry (red) and AglZ-YFP (green) as a function of time before (negative time) and after (positive time) the cell moved away from the focal adhesion position ($n = 10$; two technical replicates). **b**, Predicted domain architecture of the Agl–Glt machinery based on bioinformatics prediction, sequence analysis and previous literature. The different proteins of the complex are represented on the basis of their domain structures from bioinformatics predictions (Supplementary Table 1). Each protein is represented as a single copy in the complex. **c**, A fixed contractile zone is observed in motile sporulating cells where peptidoglycan is profoundly remodelled. Motile cells in the early phases of sporulation are shown at 1-min intervals. AglQ-sfGFP and GltC-mCherry are specifically enriched at the constriction site. Representative wild-type ($n = 10$), AglQ-sfGFP ($n = 2$, two technical replicates) and GltC-mCherry ($n = 4$, two technical replicates) cells are shown, obtained from two biological replicates. **d**, Possible mechanism of propulsion. The structure of the Agl–Glt machinery is simplified to its core components for clarity. The proton flow through a peptidoglycan-bound TolQR-type channel (yellow) is proposed to energize cyclic interactions between a flexible inner membrane-anchored periplasmic protein (GltG/J, black and yellow) and TonB-box proteins in the outer membrane (orange). Combined with the rigid anchoring to peptidoglycan and link with MreB, this activity would push the outer membrane protein laterally (red arrow) because peptidoglycan counteracts the exerted traction force (grey arrow). The protein stoichiometries are not known and it is possible that the complex contains several coordinated legs, facilitating the processivity and directionality of the movements.

Adhesion and cyclic OM–IM contacts observed at FAS

A clear prediction of this model is that the motility complex should require direct adhesive contacts with the underlying surface to propel the cell. Consistent with this prediction, reflection interference contrast microscopy (RICM) revealed that motile cells are uniformly in contact with the substratum and high RICM densities were correlated with the position of AglZ-YFP clusters (Extended Fig. 5d). Notably, vesicles containing only outer membrane materials and specific outer membrane Glt proteins (GltC-mCherry) were deposited at sites coinciding with the positions of focal adhesion complexes in the wake of motile cells (Fig. 5a and Extended Data Fig. 5e, f). Overall, these data suggest that adhesions involve strong, intimate contacts between the surface and the periplasm–outer membrane complex.

To gain molecular insight into the mechanisms involved in force generation and surface adhesion, we predicted a protein-domain structure of the motility complex using bioinformatics approaches (Fig. 5b and Extended Data Figs 8, 9). Remarkably, both AglQ and AglS contain predicted TolR-like PG-binding motifs¹² and AglR, a TolQ homologue interacts with GltG² a TolA/TonB-like protein (Extended Data Fig. 8a–b). GltG and GltJ are similar modular proteins, specifically sharing a single transmembrane helix, a periplasmic helical domain, and TonBC motifs¹³. Interactions of GltGJ with OM components could occur between their TonBC domains and potential TonB-box-carrying proteins –GltF in the periplasm (Extended Data Fig. 8a) and GltAB, two predicted porin-like β -barrel proteins in the OM (Extended Data Fig. 9a–b).

Thus, peptidoglycan-anchored Agl motor units may act as stators, pushing against adhesive outer membrane complexes through peptidoglycan to generate propulsive forces. We reasoned that these dynamic interactions might be revealed under conditions in which the rigidity of the cell envelope is reduced, for example in cells undergoing sporulation where rapid peptidoglycan remodelling leads to the formation of round cells¹⁴. Indeed, the induction of sporulation rapidly led to the formation of balloon-shaped cells (Fig. 5c). Notably, a small fraction of cells (<1%) entering sporulation were still motile and formed conspicuous constrictions that, similar to focal adhesion complexes, remained fixed relative to the surface (Fig. 5c). These constrictions probably resulted from the activity of the Agl–Glt machinery because: (i) they formed only in motile sporulating cells (<1% of the sporulating cell population); and (ii) both AglQ-sfGFP (inner membrane) and GltC-mCherry (outer membrane) were enriched at constriction sites (Fig. 5c). Thus, in sporulating cells where the structure of peptidoglycan is different (peptidoglycan is not detected in mature spores¹⁵), dynamic Agl–Glt-driven physical contacts between the outer membrane and the inner membrane are unmasked.

Discussion

On the basis of our results, we propose that the Agl motor and associated inner membrane proteins move directionally by cyclic interactions with factors in the periplasmic–outer membrane complex (Fig. 5d). Analogous to Tol-Exb systems^{13,16}, these steps would occur by PMF-driven conformational changes in the Glt TolA/TonB-like proteins (GltG and/or GltJ; Fig. 5b), the flexible domains of which might extend and retract through the peptidoglycan layer (Fig. 5d). Peptidoglycan itself could act as both a transient anchor point, as it becomes bound by AglQ/S via a TolR-like peptidoglycan-binding motif, and a guiding factor, as it opposes contractions to favour lateral movements (Fig. 5d).

The current study does not resolve the relative stoichiometries of the Agl and Glt proteins at focal adhesions, but the data show that the activity of focal adhesion complexes is subject to regulation and contains variable stoichiometries of Agl motor components and connections with the underlying surface. Thus, it is possible that several ‘legs’ operate coordinately at these sites. The directionality of motility complexes is remarkably consistent between cells, suggesting that a core cellular structure is involved; peptidoglycan is an attractive candidate because the glycan strands are proposed to have a global right-handed helical ordering that could serve as tracks to guide the motility complex¹⁷. At FASs, the interaction with the surface appears to be strong, implying the existence of one or more specific adhesion molecule(s); consequently, there is likely to be a relief mechanism similar to that found in gliding parasites, where the major adhesion molecule is removed from the motility complex by specific proteolysis¹⁸. In addition, our model makes several important predictions that will help future studies, such as the systematic exploration of protein interactions in the system to attain a molecular understanding of the motility mechanism.

Online Content Methods, along with any additional Extended Data display items and Source Data, are available in the online version of the paper; references unique to these sections appear only in the online paper.

Received 21 March; accepted 28 September 2016.

Published online 5 October 2016.

1. Islam, S. T. & Mignot, T. The mysterious nature of bacterial surface (gliding) motility: A focal adhesion-based mechanism in *Myxococcus xanthus*. *Semin. Cell Dev. Biol.* **46**, 143–154 (2015).
2. Luciano, J. et al. Emergence and modular evolution of a novel motility machinery in bacteria. *PLoS Genet.* **7**, e1002268 (2011).
3. Sun, M., Wartel, M., Cascales, E., Shaevitz, J. W. & Mignot, T. Motor-driven intracellular transport powers bacterial gliding motility. *Proc. Natl Acad. Sci. USA* **108**, 7559–7564 (2011).
4. Jakobczak, B., Keilberg, D., Wuichet, K. & Søgaard-Andersen, L. Contact- and protein transfer-dependent stimulation of assembly of the gliding motility machinery in *Myxococcus xanthus*. *PLoS Genet.* **11**, e1005341 (2015).
5. Nan, B. et al. Myxobacteria gliding motility requires cytoskeleton rotation powered by proton motive force. *Proc. Natl Acad. Sci. USA* **108**, 2498–2503 (2011).
6. Balagam, R. et al. *Myxococcus xanthus* gliding motors are elastically coupled to the substrate as predicted by the focal adhesion model of gliding motility. *PLOS Comput. Biol.* **10**, e1003619 (2014).
7. Treuner-Lange, A. et al. The small G-protein MglA connects to the MreB actin cytoskeleton at bacterial focal adhesions. *J. Cell Biol.* **210**, 243–256 (2015).
8. Nan, B. et al. Flagella stator homologs function as motors for myxobacterial gliding motility by moving in helical trajectories. *Proc. Natl Acad. Sci. USA* **110**, E1508–E1513 (2013).
9. Kaiser, D. & Warrick, H. Transmission of a signal that synchronizes cell movements in swarms of *Myxococcus xanthus*. *Proc. Natl Acad. Sci. USA* **111**, 13105–13110 (2014).
10. Bean, G. J. et al. A22 disrupts the bacterial actin cytoskeleton by directly binding and inducing a low-affinity state in MreB. *Biochemistry* **48**, 4852–4857 (2009).
11. Huang, B., Wang, W., Bates, M. & Zhuang, X. Three-dimensional super-resolution imaging by stochastic optical reconstruction microscopy. *Science* **319**, 810–813 (2008).
12. Wojdyla, J. A. et al. Structure and function of the *Escherichia coli* Tol-Pal stator protein TolR. *J. Biol. Chem.* **290**, 26675–26687 (2015).
13. Gresock, M. G., Kastead, K. A. & Postle, K. From homodimer to heterodimer and back: elucidating the TonB energy transduction cycle. *J. Bacteriol.* **197**, 3433–3445 (2015).
14. Wartel, M. et al. A versatile class of cell surface directional motors gives rise to gliding motility and sporulation in *Myxococcus xanthus*. *PLoS Biol.* **11**, e1001728 (2013).
15. Bui, N. K. et al. The peptidoglycan sacculus of *Myxococcus xanthus* has unusual structural features and is degraded during glycerol-induced myxospore development. *J. Bacteriol.* **191**, 494–505 (2009).
16. Cascales, E., Gavioli, M., Sturgis, J. N. & Lloubès, R. Proton motive force drives the interaction of the inner membrane TolA and outer membrane pal proteins in *Escherichia coli*. *Mol. Microbiol.* **38**, 904–915 (2000).
17. Wang, S., Furchtgott, L., Huang, K. C. & Shaevitz, J. W. Helical insertion of peptidoglycan produces chiral ordering of the bacterial cell wall. *Proc. Natl Acad. Sci. USA* **109**, E595–E604 (2012).
18. Ejigiri, I. et al. Shedding of TRAP by a rhomboid protease from the malaria sporozoite surface is essential for gliding motility and sporozoite infectivity. *PLoS Pathog.* **8**, e1002725 (2012).
19. den Blaauwen, T., de Pedro, M. A., Nguyen-Distèche, M. & Ayala, J. A. Morphogenesis of rod-shaped sacculi. *FEMS Microbiol. Rev.* **32**, 321–344 (2008).
20. Nan, B., Mauriello, E. M. F., Sun, I.-H., Wong, A. & Zusman, D. R. A multi-protein complex from *Myxococcus xanthus* required for bacterial gliding motility. *Mol. Microbiol.* **76**, 1539–1554 (2010).

Supplementary Information is available in the online version of the paper.

Acknowledgements We thank R. Mercier for suggestions and critical reading of the manuscript, A. Valeri for help with PCA analysis, C. Fiche for help with image analysis and Y. Denis (IMM transcriptomics platform) for help with quantitative PCR and M. Wartel for preliminary experiments. L.M.F. was partially funded by Fondation ARC, L.E. was supported by the Fondation pour la Recherche Médicale (FRM DGE2010221257), S.T.I. was supported by a fellowship from the Canadian Institutes of Health Research and the AMIDEA program of Aix-Marseille Université, and A.L. and V.A. were supported by the IRP funds of the NIH, NIH grant GM113172 to M.S.V.N. and Y.V.B. and NIH grant GM51986 to Y.V.B. Research in the Mignot laboratory was supported by European Research Council grant DOME-261105 and a Bettencourt-Schueller “Coup d’élán pour la recherche Française 2011”. Research in the Nollmann laboratory was supported by ANR grants IBM (ANR-14-CEO9-0025-01), HiResBacs (ANR-15-CE11-0023), and European Research Council grant smInsulator-260787. We acknowledge support from France-BioImaging (ANR-10-INBS-04, “Investments for the future”), and Imagine Optic.

Author Contributions L.M.F., J.-B.F., L.E., M.N. and T.M. conceived the experiments and analysed the data with help from A.D. for TADA experiment analysis. L.M.F. and J.-B.F. performed most of the experiments, including TIRF assays, astigmatism and strain construction. A.D. and S.L. helped with TADA experiments. J.L., M.S., and S.L. constructed strains. S.T.I., J.T. and O.T. performed RICM studies. V.A. and A.L. performed bioinformatics analysis. E.K., M.S.V.N. and Y.V.B. provided TADA. M.N. and T.M. wrote the paper with help from L.M.F., J.-B.F. and L.E.

Author Information Reprints and permissions information is available at www.nature.com/reprints. The authors declare no competing financial interests. Readers are welcome to comment on the online version of the paper. Correspondence and requests for materials should be addressed to T.M. (tmignot@imm.cnrs.fr) or M.N. (marcelo.nollmann@cbs.cnrs.fr).

Reviewer Information *Nature* thanks J. Armitage, P. Kukura and the other anonymous reviewer(s) for their contribution to the peer review of this work.

METHODS

Bacterial strains, plasmids, and growth. Strains, primers, and plasmids are listed in Supplementary Tables 2 and 3. See Supplementary Tables 2 and 4 for strains and their mode of construction. *M. xanthus* strains were grown at 32 °C in casitone yeast extract (CYE)-rich medium as previously described²¹. Plasmids were introduced into *M. xanthus* by electroporation. Mutants and transformants were obtained by homologous recombination based on a previously reported method²¹. All fusions were expressed by gene replacement at the endogenous loci allowing expression from the natural promoters. Quantitative PCR experiments confirmed that expression was similar to wild-type levels (expression ratios varied between 1 and 2 compared to wild-type levels). Three types of AglQ fusion were used throughout the study: TIRF experiments used AglQ-mCherry expressed from the endogenous locus in place of the wild-type gene. For technical reasons, the PCA analysis and expression of AgQ-sfGFP used fusions expressed after ectopic integration of the gene of interest at the Mx8-phage attachment site in a Δ aglQ deletion background (Supplementary Table 4). All three strains were indistinguishable in terms of motility and expression patterns. *Escherichia coli* cells were grown under standard laboratory conditions in Luria–Bertani broth supplemented with antibiotics, if necessary.

Motility assays on agar surfaces. For standard phase-contrast and fluorescence microscopy, cells from exponentially growing cultures were transferred to a 1.5% agar pad with TPM buffer (10 mM Tris-HCl, pH 7.6, 8 mM MgSO₄, and 1 mM KH₂PO₄) on a glass slide and covered with a coverslip. Imaging was performed in a temperature-adjusted microscope chamber at 32 °C. To test the function of peptidoglycan during motility, sporulation was induced by adding 5% glycerol directly into the agar pads as previously described¹⁴. This treatment induces rapid and controlled degradation of the *Myxococcus* peptidoglycan leading to the formation of viable spheroplasts¹⁴. Cells were imaged 15 min after deposition on a glycerol pad in order to image their motility while converting to spheroplasts.

Microfluidics on chitosan-coated glass slides. *M. xanthus* cells were immobilized on a chitosan-coated surface, as described previously²². In brief, custom-built poly-dimethylsiloxane microfluidic glass chambers were coated with chitosan solution and washed after 30 min. Chambers were further rinsed with 1 ml TPM buffer (10 mM Tris-HCl, pH 7.6, 8 mM MgSO₄, 1 mM KH₂PO₄). Subsequently, 1 ml of an exponentially growing culture was injected into the chamber and left for 30 min without flow. Unattached cells were removed by rinsing with 1 ml TPM buffer by manual injection and time-lapse microscopy on attached cells was performed. When needed, A22 (Merck Millipore) was injected manually at indicated concentrations a few minutes after the cells were confirmed to be motile.

Labelling cells with fluorescent D-amino acids. Lyophilized TADA (molecular mass = 381.2 g/mol) powder was re-suspended in DMSO at 150 mM and conserved at -20 °C. The labelling was performed for 2 h at 32 °C, using 2 μ l TADA solution for 1 ml cell culture ($OD_{600} = 0.5$) in the presence of 1 M NaCl for a duration of 2 h. The sample was then washed four times with 1 ml TPM buffer and finally resuspended at $OD_{600} = 5$ before being transferred to an agar pad.

Bioinformatics analyses. Iterative sequence profile searches were performed using the PSI-BLAST²³ and JACKHMMER²⁴ programs run against the non-redundant protein database of National Center for Biotechnology Information (NCBI). Similarity-based clustering for both classification and culling of nearly identical sequences was performed using the BLASTCLUST program (<ftp://ftp.ncbi.nlm.nih.gov/blast/documents/blastclust.html>). The HHpred program was used for profile-profile comparisons²⁵. Structure similarity searches were performed using the DALI Lite program²⁶. Multiple sequence alignments were built by the Kalign and PCMA programs^{27,28}, followed by manual adjustments on the basis of profile-profile and structural alignments. Secondary structures were predicted using the JPred program²⁹. For previously known domains, the Pfam database was used as a guide³⁰, and the profiles were augmented by addition of newly detected divergent members that were not detected by the Pfam models. Clustering with BLASTCLUST followed by multiple sequence alignment and further sequence profile searches were used to identify other domains that were not present in the Pfam database. Signal peptides and transmembrane segments were detected using the TMHMM and Phobius programs^{31,32}. Contextual information from prokaryotic gene neighbourhoods was retrieved using custom Perl scripts that extract the upstream and downstream genes of the query gene, along with their orientation, from GenBank files. A combination BLASTCLUST and sequence profile searches were then used to cluster the proteins to identify conserved gene-neighbourhoods. Structural visualization and manipulations were performed using the PyMol (<http://www.pymol.org>) program. The in-house TASS package, which comprises a collection of Perl scripts, was used to automate aspects of large-scale analysis of sequences, structures and genome context.

Epifluorescence microscopy. For regular epifluorescence, GFP or mCherry fluorochromes were visualized at 32 °C using a temperature-controlled TE2000-

E-PFS microscope (Nikon) with a 100× NA 1.3 (PhC) objective and a CoolSNAP HQ2 camera (Photometrics). All fluorescence images were acquired with appropriate filters with a minimal exposure time to minimize bleaching and phototoxicity effects. Images were recorded with Metamorph software (Molecular Devices).

TIRFM. TIRFM was performed with an inverted microscope (Axio Observer A1, Zeiss) equipped with a 100× Plan-Achromat oil-immersion objective (NA = 1.46) mounted on a closed-loop piezoelectric stage (PIFOC, Physik Instrumente). Two lasers with excitation wavelengths of 488 nm (OBIS 488LS, Coherent USA) and 561 nm (Sapphire 561LP, Coherent USA) were used for YFP and mCherry imaging, respectively. Laser beams were combined and collimated by a series of dichroic mirrors and achromatic lenses, individually controlled by an acousto-optic tunable filter (AOTF, AA Opto-electronic) and focused onto the back focal plane of the objective through the rear port of the microscope. A translation stage was used to shift the positions of the two beams with respect to the objective, enabling an easy permutation between Epi and TIRF imaging (Applied Scientific Instrumentation). The fluorescence emission signal was collected by the objective lens, separated from the excitation wavelengths through a four-band dichroic mirror and filtered using bandpass filters inserted in a high-speed motorized filter wheel (Chroma Technology). The filtered emission signal was then imaged onto an emCCD camera (Andor Ixon 897) through relay lenses allowing an effective pixel size of 105 nm. Along a separate path, a 785-nm infrared laser beam was focused on the back focal plane of the objective and reached the glass-sample interface in total internal reflection conditions. The reflected infrared beam was imaged by a CMOS camera (Thorlabs Inc.) and its position calculated during live acquisition. The information was fed-back to a z-positioning piezo stage through PID software to correct for any change in the objective-sample distance. This active autofocus system locks the focal plane position with a precision of ± 20 nm over hours. All acquisition software controlling lasers, filter wheel, translation stages and cameras were homemade using LabView 2012 (National Instruments). For time-lapse imaging, a high-speed motorized filter wheel was used to sequentially image YFP and mCherry channels with a switching time of less than 200 ms. Typically, 5–10 images were acquired at 20 Hz for each channel and the process was repeated 45–50 times every 15–30 s, depending on the cell speed. For real-time imaging, 500 images were taken at 20 Hz in the YFP channel. Laser intensity was optimized to get the best signal-to-noise ratio (SNR) while limiting photobleaching and phototoxicity. In order to compensate for chromatic aberrations, each channel was assigned a specific setpoint for the autofocus depending on the position of the focal planes for YFP and mCherry fluorescence signals.

Astigmatism for 3D time-lapse experiments. First, analysis of TADA-bright clusters by epifluorescence showed that they are diffraction limited and circular in shape, making their 3D tracking by astigmatism possible. 3D imaging was performed as previously described³³. Briefly, to obtain 3D imaging conditions, a corrective MicAO 3D-SR system (Imagine Optic) was inserted into the emission pathway between a modified Nikon Eclipse Ti-S inverted microscope and an EMCCD camera (Andor Ixon 897). A MicAO 3D-SR adaptive optics device was used to correct the microscope point spread function (PSF) for optical aberrations introduced in the imaging path and to optimize the photon budget. For 3D detection, subtle changes in astigmatism were further added in order to break the axial symmetry of the PSF and allow an estimation of the axial position of diffraction-limited fluorescent objects. Time-lapse imaging of TADA clusters was performed after transferring to an agar pad freshly labelled cells mixed with 100-nm fluorescent beads (TetraSpeck, Thermo Scientific), used as fiducial and calibration markers. Every 15–30 s, two series of 5–10 successive images were simultaneously acquired at 20 Hz: one under continuous epifluorescence illumination with a 561-nm read-out laser to detect the fluorescence of the TADA clusters (Sapphire 561LP, 150 mW, Coherent) and the second using a brightfield illumination to get an image of the cells. Then, a calibration was performed on the same field of view by imaging single fluorescent beads while scanning the sample along the optical axis (z) by steps of 50 nm.

Detection and quantification of TADA clusters is described below. In total, data from eight cells were successfully analysed (five biological replicates). However, the behaviour described was clearly observed on numerous occurrences ($n = 10$), though the data were not of high enough quality (low SNR, cell to cell contact, cell moving too quickly or out of the observation field and so on) to obtain long trajectories.

RICM. For label-free imaging of the underside of cells in contact with the substratum, a modified form of reflection imaging for bacteria was employed³⁴. RICM was performed on chitosan-coated microfluidic chambers. Chambers were seeded with Δ pilA cells expressing AglZ-YFP resuspended in TPM buffer with 1 mM CaCl₂ ($OD_{600} = 0.5$) for 10 min, then washed with the same buffer. Images were obtained at 32 °C on a Zeiss Axiovert 200 inverted microscope

with adjustable aperture and field stops. For imaging, an RICM objective (Zeiss Neofluar 63/1.25 antiflex) and a differential interference contrast objective (Plan-Apochromat 63 \times 1.40 oil) were used for crossed-polarized light and fluorescence images, respectively. For RICM, cells were illuminated through a 546 \pm 12 nm narrow bandpass filter with a mercury lamp (X-cite 120Q lamp) for 20 ms. For fluorescence, samples were excited with a laser at 488 nm for 1,000 ms. Images were captured at 10-s intervals and combined in ImageJ.

Fluorescence recovery after photobleaching (FRAP). FRAP was performed with a 488-nm laser mounted directly on the TE2000-E-PFS microscope (Nikon), allowing us to focus a micrometre-radius laser beam with micrometre precision. FRAP acquisitions were performed with a home-developed macro under Metamorph.

Cluster image analysis. Trajectories of fluorescent clusters were obtained from the coordinates calculated in a cylindrical reference system based on the shape of the cell. This step was performed automatically and verified manually using the MicrobeJ plugin (<http://www.indiana.edu/~microbej/>) in FIJI/ImageJ³⁵. These coordinates were used to calculate angle, speeds, mean square displacements and angles using R software. To calculate the slope of helicoidal trajectories, the unwrapped coordinates were fitted with a linear regression model and φ angles were determined as the arctangent of the line coefficient (Extended Data Fig. 2e). In TIRFM, owing to the narrow depth of focus, different fluorescent objects (AglZ-YFP) were treated as if they were in the same plane. This simplified the method of calculating the trajectory angles. A z-stack projection of maxima was applied (FIJI). Some cells in the projection image showed clear linear alignments of clusters crossing the cell body. The angle between the linear clusters trajectory and the major axis of the cell was manually measured with the angle tool of the FIJI software.

Principal component analysis. The number of clusters and the relative positions of AglZ-YFP, GltI-YFP and AglQ-mCherry in *agl:gt* mutant backgrounds were obtained by combining the mask of cells obtained from phase contrast images and the fast Fourier transform (FFT)-filtered fluorescent image (FIJI, Extended Data Fig. 3b). In brief, the phase-contrast image of rod-shaped cells provides a mask of cell bodies and yields morphological parameters and definition of the longitudinal axis. Following a straightening operation, this axis can be used as a reference frame for cluster localization. Because the internal clusters are of weak intensity, the images were denoised by applying a neutral density filter and background subtraction. The presence of fluorescent clusters was systematically verified on unprocessed images to ensure that the procedures did not generate artefactual signals. The following list provides the number of cells analysed for each condition resulting from six technical replicates. For the AglZ-YFP reporter: wild-type, 67; $\Delta gltA$, 146; $\Delta gltB$, 407; $\Delta gltC$, 224; $\Delta gltD$, 139; $\Delta gltE$, 168; $\Delta gltF$, 136; $\Delta gltG$, 323; $\Delta gltH$, 114; $\Delta gltI$, 193; $\Delta gltJ$, 174; $\Delta gltK$, 194; $\Delta gltQ$, 407. For the GltI-YFP reporter: wild-type, 187; $\Delta gltA$, 688; $\Delta gltB$, 292; $\Delta gltC$, 321; $\Delta gltD$, 133; $\Delta gltE$, 296; $\Delta gltF$, 114; $\Delta gltG$, 64; $\Delta gltH$, 261; $\Delta gltJ$, 359; $\Delta gltK$, 694; $\Delta gltQ$, 187. For the AglQ-mcherry reporter: wild-type, 163; $\Delta gltA$, 124; $\Delta gltB$, 723; $\Delta gltC$, 266; $\Delta gltD$, 201; $\Delta gltE$, 399; $\Delta gltF$, 196; $\Delta gltG$, 189; $\Delta gltJ$, 511; $\Delta gltK$, 197.

Two-colour TIRFM. Image analysis was performed using Matlab 2015 (MathWorks). For each experiment, only cells displaying gliding displacement were analysed. For each selected bacterium, a temporal RGB image was calculated using mCherry fluorescence images and the cell trajectory path was manually drawn (Extended Data Fig. 6a). A montage and its associated kymograph were then calculated for both YFP and mCherry channels by straightening and re-slicing each time-lapse image along that path (Extended Data Fig. 6b). For the kymograph, the best contrast was obtained by averaging the intensity of the three brightest pixels (over a total of 13 pixels) for each slice. To further improve the contrast of the kymographs and highlight the presence of fluorescent clusters, a denoising algorithm (modified from ref. 36) was applied (Extended Data Fig. 6c). Photobleaching was also quantified for each channel based on the variation of non-specific fluorescence signal measured in the cells over time. A single exponential model was used to fit the variation of intensity and correct the kymograph intensity accordingly. Small shifts induced by chromatic aberrations between the two channels were corrected as well by realigning the two kymographs using an image cross-correlation algorithm (precision of 1 pixel, 105 nm). Finally, for the co-localization calculation, the intensities of both images were standardized in order to compare the fluorescent signals from both YFP and mCherry channels.

Cell tracking in kymographs. To calculate the cell displacement over time, the kymograph displaying the best contrast was first interpolated: the number of pixels was increased by twofold in each dimension and the intensity of each pixel recalculated using a cubic interpolation algorithm. An iterative edge-detection algorithm based on the Canny method was then applied to the interpolated image³⁷. Typical values for the standard deviation were between 3 and 5 pixels. By iteratively changing the Canny detection threshold, the algorithm converged towards two

different edges highlighting the movement of both cell poles during the time-lapse. Errors in the edge calculation were sometimes observed when the lagging pole of the cell was not properly attached to the chitosan-treated surface and/or when other bacteria were in contact with the selected cell. In that case, a manual correction was performed in order to remove inconsistent points and rectify the position of the edges.

Often, the two edges were not exactly identical owing to imprecision in the localization of poles. Indeed, we could observe that the leading pole of the cell was usually very well defined (highest fluorescence intensity) resulting in a very precise calculation of its localization over time. On the contrary, the lagging pole was often poorly defined due to lower fluorescence intensity and/or weaker adhesion to the chitosan-treated surface. Therefore, in order to quantify the cell displacement during the time-lapse, the edge defined with the highest precision was selected. The speed was also estimated from the first derivative of the displacement and analysed in order to automatically identify when the cell was mobile (gliding) during the time-lapse acquisition. To do so, for each experiment, a velocity threshold was empirically estimated by analysing the movement of a small subset of cells. Then, for each time-point, bacteria were classified as either mobile or immobile depending on whether their velocity surpassed the velocity threshold. Typical values for the threshold lay between 0.05 and 0.2 $\mu\text{m}/\text{min}$, depending on experimental drift and noise (Extended Data Fig. 6d). In average, cell speed on the chitosan-coated surface was $0.5 \pm 0.5 \mu\text{m}/\text{min}$.

Co-localization. Co-localization between YFP-tagged and mCherry-tagged proteins was calculated in three steps (Extended Data Fig. 7a). First, the two montages were separately analysed in order to localize the fluorescent clusters in each channel. For each montage, its normalized cross-correlation with a Gaussian spot (s.d. of 1 pixel) was computed. Fluorescent aggregates were then delimited by thresholding the image (typical value 0.55–0.75) and grouping the selected pixels in separate clusters based on their connectivity. Clusters composed of fewer than 4 pixels were systematically discarded.

In a single cell, many different fluorescent clusters $C_{n=1,2,\dots}$ could be simultaneously detected, each with a different trajectory. As the same fluorescent cluster C_n could be detected in several successive images, localizations were grouped by manually stitching together its detections ($C_n^{t_1}, C_n^{t_1+1}, \dots, C_n^{t_1+k}$) on the montage. Therefore, each cluster $C_{n=1,2,\dots}$ was now defined by all its localizations during the time-lapse acquisition. By analysing their positions over time, each observation of the same cluster was labelled as either stationary or dynamic. Finally, it is important to point out that clusters detected at the poles were not taken into account for the analysis. The pixel size in our experiments was 105 nm; thus, the precision of detection of the maximum of intensity of clusters from kymographs was approximately ~ 100 nm.

Next, for each montage, the localizations of the clusters were projected onto the associated normalized kymograph. A protein detection map was then calculated by keeping only the intensities of the pixels that were part of a cluster (Extended Data Fig. 7b). The intensity of all other pixels was set to zero. By superimposing the trajectories of the two cell poles, it was then possible to study how the detection of protein clusters was correlated with cell displacement. Each row of the map corresponded to a snapshot of the protein localization and intensity within the cell at a given time of the experiment. Finally, the co-localization map was calculated by multiplying the two detection maps together (Extended Data Fig. 7c). From the distinction performed earlier between stationary and dynamic clusters, we could measure how the co-localization intensity varied over time for both types of clusters. Two curves were therefore calculated by summing along each row the intensity of the pixels associated to either dynamic or stationary clusters. In the end, the total co-localization signal was obtained by summing together the two curves.

Correlation between cell movement and co-localization. For each cell, correlation between movement and protein co-localization was calculated, taking static and dynamic clusters into account separately (Extended Data Fig. 7d, e). For each time-point, the correlation was set to 1 when the cell was mobile and co-localization was detected or when the cell was immobile and no co-localization was measured. In all the other cases, the correlation was set to -1 (Extended Data Fig. 7f). Then, a correlation score was attributed to each cell and each type of cluster (stationary or dynamic) by calculating the mean of all the values over time.

To further estimate the connection between cell movement and protein co-localization, a more quantitative analysis was performed. For each cell, speeds were first renormalized between 0 (no movement) and 1 (maximum velocity) and segmented into 15 equally spaced bins. Next, for each bin, we selected all the occurrences associated to a moving cell and verified whether static or dynamic co-localized clusters were detected. By repeating this analysis on all cells, we could therefore estimate for each bin the percentage of events where co-localization was detected. Finally, the percentage of co-localization was plotted separately for static and dynamic clusters as a function of the normalized cell speed.

Correlation between cell movement and cluster fluorescence intensity. To investigate the connection between cell movement and protein recruitment at focal adhesion complexes, we analysed how the intensity of AglZ and AglQ clusters changed with cell speed. Owing to cell-to-cell variability in the measured fluorescence signal, the intensity of static clusters was renormalized for each cell. For the cells displaying at least one dynamic cluster, the maximum intensity of dynamic clusters was calculated and used as an internal reference to normalize the intensity of all detected clusters within the cell. Behind this normalization procedure, we make the assumption that dynamic clusters have on average the same stoichiometry or composition from cell to cell. This assumption was verified since, after analysing more than 100 cells for AglZ and AglQ proteins, the intensity measured after normalization for the dynamic clusters showed a very small dispersion (mean intensity of 1 ± 0.15 for AglZ and AglQ) while the dispersion for the static clusters was about three times higher (mean intensity of 1.38 ± 0.5 for AglZ and 1.4 ± 0.43 for AglQ). Then, as already described for the correlation between cell movement and co-localization, we plotted the intensity of both static and dynamic clusters as a function of the normalized cell speed.

Note that this analysis could only be performed for AglZ and AglQ, as in this case the proportion of cells displaying both dynamic and static clusters was large enough to obtain a statistically relevant sample size (59% for AglZ and 64% for AglQ). For GltC and GltD, however, very few dynamic clusters were detected and these proportions dropped to 5% and 8%, respectively, which was insufficient for performing a similar analysis.

Analysis of TADA clusters by astigmatism. Detection of beads from the calibration were analysed using RapidSTORM³⁸. For each axial position (z) of the sample, the PSF of a single fluorescent bead was fitted with an elliptical Gaussian function and the x - y widths (w_x and w_y) were calculated in order to produce the calibration curves $w_x(z)$ and $w_y(z)$.

Only gliding cells displaying a bright and well-defined TADA cluster were selected for the analysis. First, the calibration curves were used to infer the axial positions of the clusters using RapidSTORM. Then, the cell outline was calculated on each image using the bright-field images. The cell outline was used to reconstruct the complete trajectory of the cell during the time-lapse and infer the lateral position of the TADA cluster. From the trajectory, we precisely determined for each image the total distance travelled by the cell since the beginning of the acquisition. Finally, the 3D position of the TADA clusters was plotted as a function of the distance travelled by the cell.

Principal component analysis and statistical tests. The PCA analysis was performed using Matlab 2014 and the Statistics and Machine Learning Toolbox. We started by defining a data matrix C_i for each mutant (WT, dA, dB, dC, ...) and reporter (AglZ, AglQ and GltI). For example, in the case of AglZ as a reporter, we defined one array C_{WT} for the wild-type strain and twelve others ($C_{dA}, C_{dB}, C_{dC}, \dots$) for each mutant. Each row of an array C_i corresponded to a single observation of a cluster measured by fluorescence microscopy. The columns corresponded to the variables used to describe the properties of the clusters and of the associated strain: (i) longitudinal position of the cluster (0 at the leading pole, 1 at the lagging pole); (ii) lateral position (0 at the centre, 1 on the edge); (iii) total number of clusters detected simultaneously in the same cell; and (iv) proportion of cells containing at least one cluster for the selected strain and reporter.

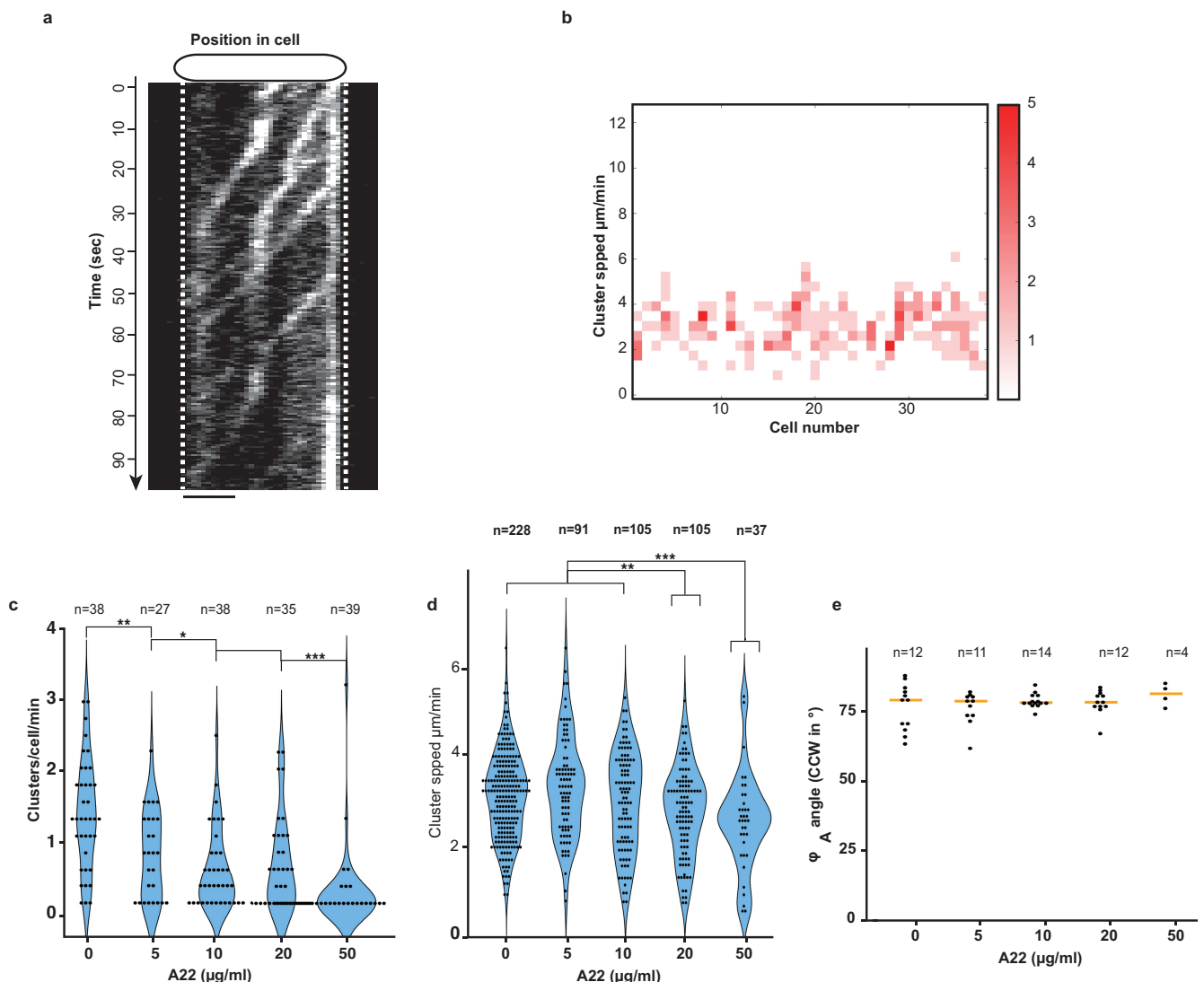
For each reporter, the PCA calculation was performed by combining all the data collected (wild-type and mutated strains). Therefore, a single set of principal components were defined and subsequently used to illustrate the differences between the wild-type and the mutated strains. The analysis was performed in three steps. First, all the data-matrices C_i were concatenated in a single matrix C_{all} and the values of each column were centred (mean was equal to 0) and standardized using the inverse variance. Then, the PCA analysis was performed and returned the coefficients of the principal components (PCs, Extended Data Fig. 4a–c) as well as the amount of variance accounted for by each of them (Extended Data Fig. 4d). Independently of the nature of the reporter, we observed that the three first components accounted for more than 87% of the total variance (>68% for the two first components). Therefore, the clusterization calculation was performed later using only the three first PCs.

In a second step, the values of the PCs were used to calculate the representations C_i^{PC} of each data-matrix C_i in the principal component space. Using a system of axes defined by the three first PCs, we could represent each array C_i^{PC} by a scatter plot in which each point represents the properties and localization of one single cluster in the PC space (Extended Data Fig. 4e). To improve the readability of the plots, we represented only the median position of each scatter plot (Extended Data Fig. 4e). We also used the standard deviation to illustrate the dispersion of the data along each PC. Finally, in order to make the comparison between wild-type and mutated strains easier, we arbitrarily placed the wild type at the origin.

Statistics and replicates. By default we used the Wilcoxon (two-sided) test to significantly separate the different samples. For each experiment, the number of times it was independently replicated in the laboratory (biological replicate) is indicated either in the figure legend or in the corresponding Methods section. All errors calculated on values were determined using the deviation standard formula.

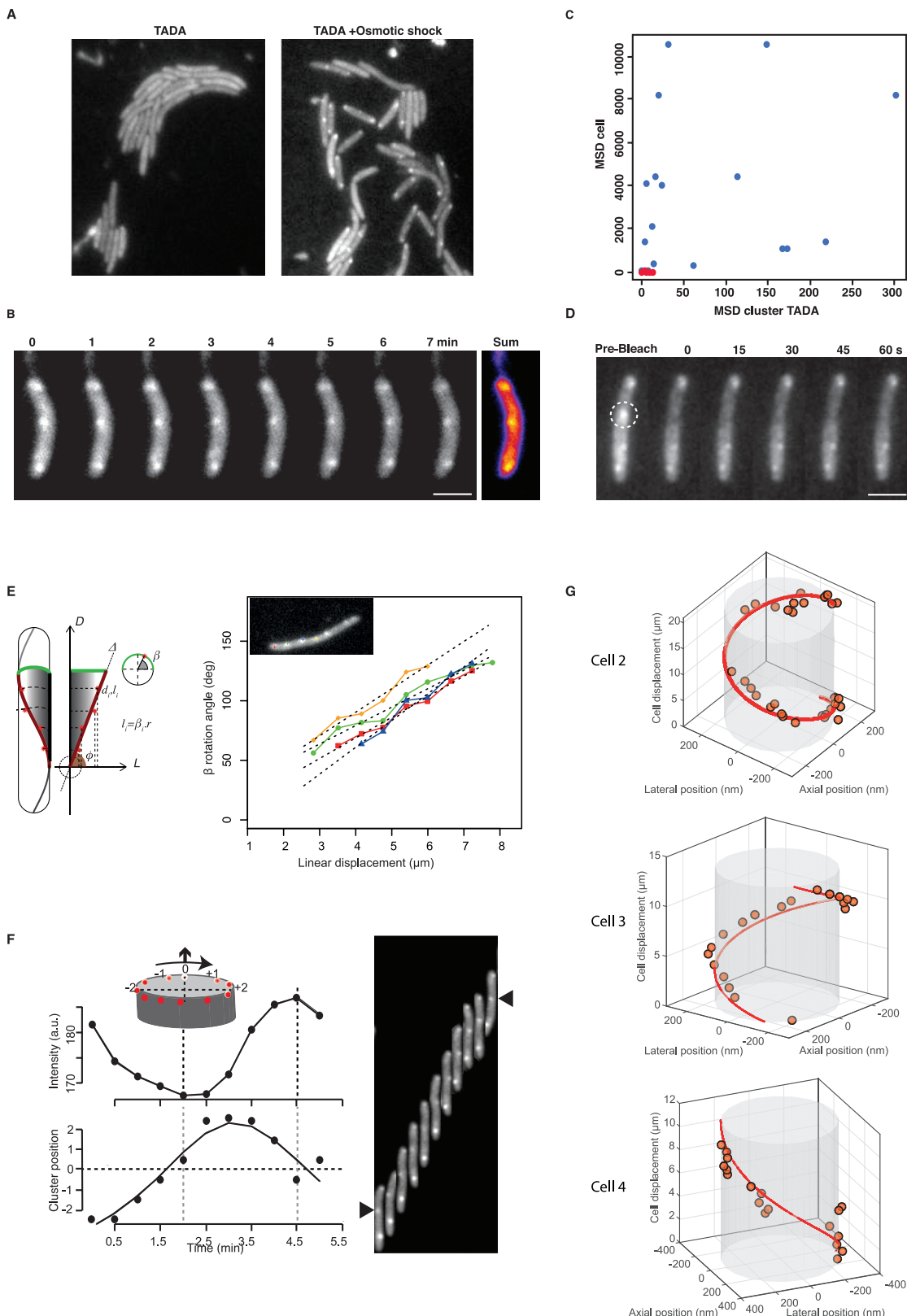
Data and code availability. Code used for two-colour TIRF and astigmatism experiments was written using Matlab 2015. Scripts are available upon request. The data that support the findings of this study are available from the corresponding author upon request.

21. Bustamante, V. H., Martínez-Flores, I., Vlamakis, H. C. & Zusman, D. R. Analysis of the Frz signal transduction system of *Myxococcus xanthus* shows the importance of the conserved C-terminal region of the cytoplasmic chemoreceptor FrzCD in sensing signals. *Mol. Microbiol.* **53**, 1501–1513 (2004).
22. Ducret, A., Théodoly, O. & Mignot, T. Single cell microfluidic studies of bacterial motility. *Methods Mol. Biol.* **966**, 97–107 (2013).
23. Altschul, S. F. et al. Gapped BLAST and PSI-BLAST: a new generation of protein database search programs. *Nucleic Acids Res.* **25**, 3389–3402 (1997).
24. Johnson, L. S., Eddy, S. R. & Portugaly, E. Hidden Markov model speed heuristic and iterative HMM search procedure. *BMC Bioinformatics* **11**, 431 (2010).
25. Söding, J., Biegert, A. & Lupas, A. N. The HHpred interactive server for protein homology detection and structure prediction. *Nucleic Acids Res.* **33**, W244–W248 (2005).
26. Holm, L., Kääriäinen, S., Rosenström, P. & Schenkel, A. Searching protein structure databases with DaliLite v.3. *Bioinformatics* **24**, 2780–2781 (2008).
27. Lassmann, T., Frings, O. & Sonnhammer, E. L. L. Kalign2: high-performance multiple alignment of protein and nucleotide sequences allowing external features. *Nucleic Acids Res.* **37**, 858–865 (2009).
28. Pei, J., Sadreyev, R. & Grishin, N. V. PCMA: fast and accurate multiple sequence alignment based on profile consistency. *Bioinformatics* **19**, 427–428 (2003).
29. Drozdetskiy, A., Cole, C., Procter, J. & Barton, G. J. JPred4: a protein secondary structure prediction server. *Nucleic Acids Res.* **43** (W1), W389–W394 (2015).
30. Finn, R. D. et al. Pfam: the protein families database. *Nucleic Acids Res.* **42**, D222–D230 (2014).
31. Krogh, A., Larsson, B., von Heijne, G. & Sonnhammer, E. L. Predicting transmembrane protein topology with a hidden Markov model: application to complete genomes. *J. Mol. Biol.* **305**, 567–580 (2001).
32. Käll, L., Krogh, A. & Sonnhammer, E. L. L. A combined transmembrane topology and signal peptide prediction method. *J. Mol. Biol.* **338**, 1027–1036 (2004).
33. Marbouty, M. et al. Condensin- and replication-mediated bacterial chromosome folding and origin condensation revealed by Hi-C and super-resolution imaging. *Mol. Cell* **59**, 588–602 (2015).
34. Ducret, A., Vallignat, M. P., Mouhamar, F., Mignot, T. & Theodoly, O. Wet-surface-enhanced ellipsometric contrast microscopy identifies slime as a major adhesion factor during bacterial surface motility. *Proc. Natl. Acad. Sci. USA* **109**, 10036–10041 (2012).
35. Schindelin, J. et al. Fiji: an open-source platform for biological-image analysis. *Nat. Methods* **9**, 676–682 (2012).
36. Arigovindan, M. et al. High-resolution restoration of 3D structures from widefield images with extreme low signal-to-noise-ratio. *Proc. Natl. Acad. Sci. USA* **110**, 17344–17349 (2013).
37. Marques, O. *Practical Image and Video Processing using MATLAB* (John Wiley & Sons, 2011).
38. Wolter, S. et al. rapidSTORM: accurate, fast open-source software for localization microscopy. *Nat. Methods* **9**, 1040–1041 (2012).



Extended Data Figure 1 | Dynamic AglZ-YFP clusters in non-motile cells. **a**, Dynamic AglZ-YFP clusters in a non-motile cell observed by TIRFM. Kymograph representation of cluster movement captured every 0.5 s. Note that the clusters form at the cell pole and move directionally towards the opposite cell pole where they are dispersed. Scale bar, 2 μm . **b**, Distribution of cluster speeds between and within cells. Note that clusters can move at different speeds in a cell and that the speed between

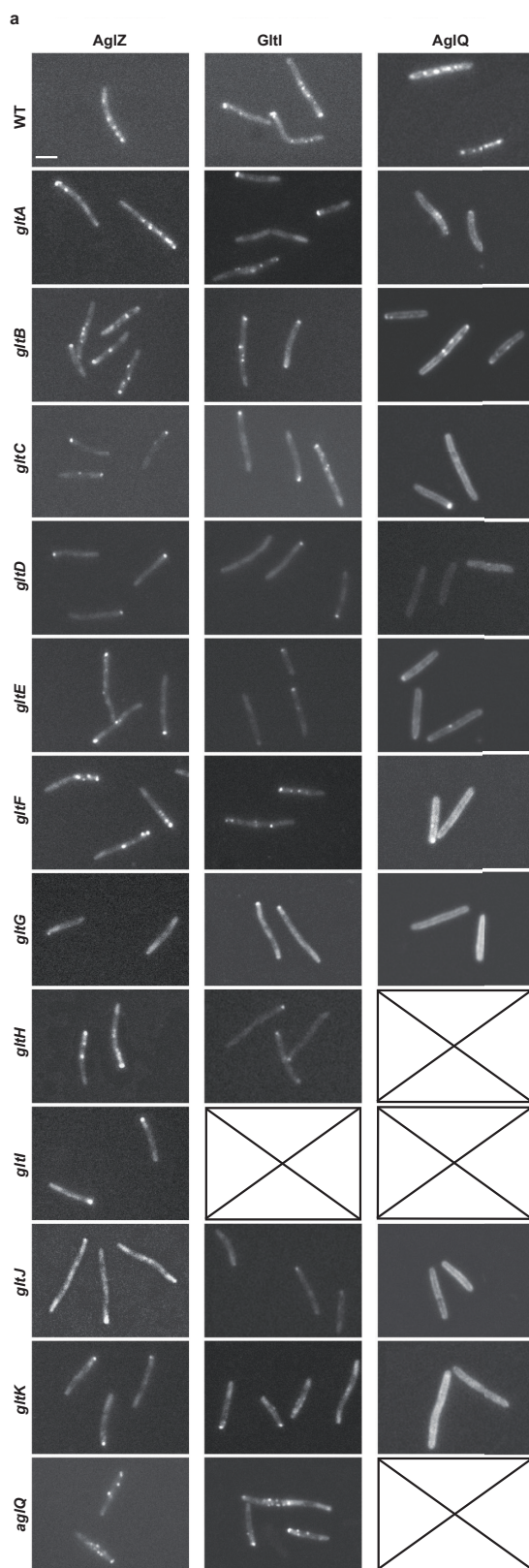
cells generally varies between 2 and 4 $\mu\text{m min}^{-1}$ (two technical replicates). **c**, Number of AglZ-YFP clusters per cell per minute in wild-type and A22-treated cells (two technical replicates). **d**, AglZ-YFP cluster speed in wild-type and A22-treated cells (two technical replicates). **e**, Trajectory angles in wild-type and A22-treated cells (two technical replicates). Wilcoxon tests; * $P < 0.1$; ** $P < 0.01$; *** $P < 0.001$ (**c–e**).



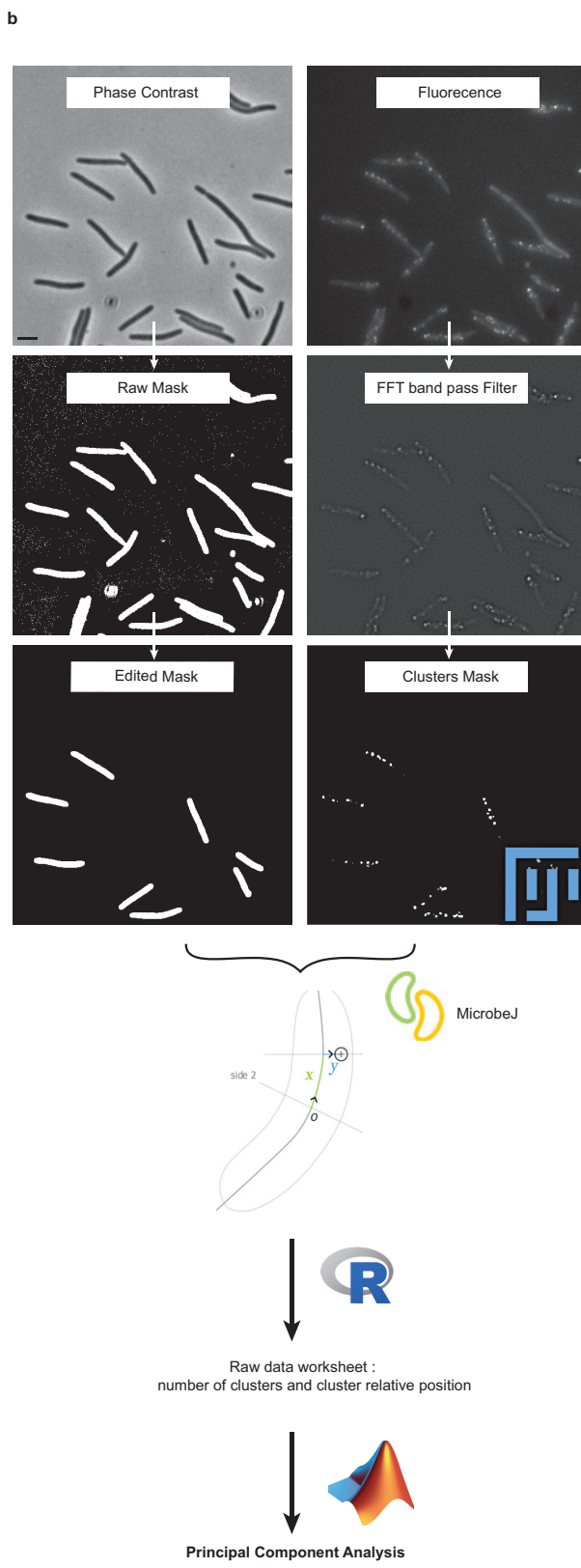
Extended Data Figure 2 | See next page for caption.

Extended Data Figure 2 | *Myxococcus* cells rotate along their long axes during motility. **a**, TADA-bright clusters form in *Myxococcus* cells subjected to a brief osmotic shock. TADA is incorporated in the *Myxococcus* cell envelope only when the cells are subjected to NaCl treatment (see Methods). **b, c**, TADA-bright clusters are not dynamic in non-motile cells. TADA-bright cluster movements are not detectable in non-motile cells (**c**, red dots, $n = 14$; two technical replicates) and only detectable in moving cells (**c**, blue dots, $n = 17$; two technical replicates). MSD, mean square displacement. Scale bar, 2 μm . **d**, TADA-bright clusters are inert. FRAP analysis reveals the absence of fluorescent molecule exchange in TADA-bright clusters ($n = 6$; one technical experiment). Scale bar, 2 μm . **e**, TADA-bright cluster rotation reflects rotation of the cell during movement. A cell on which four TADA-bright clusters were tracked is shown. The radial velocity of each cluster calculated by

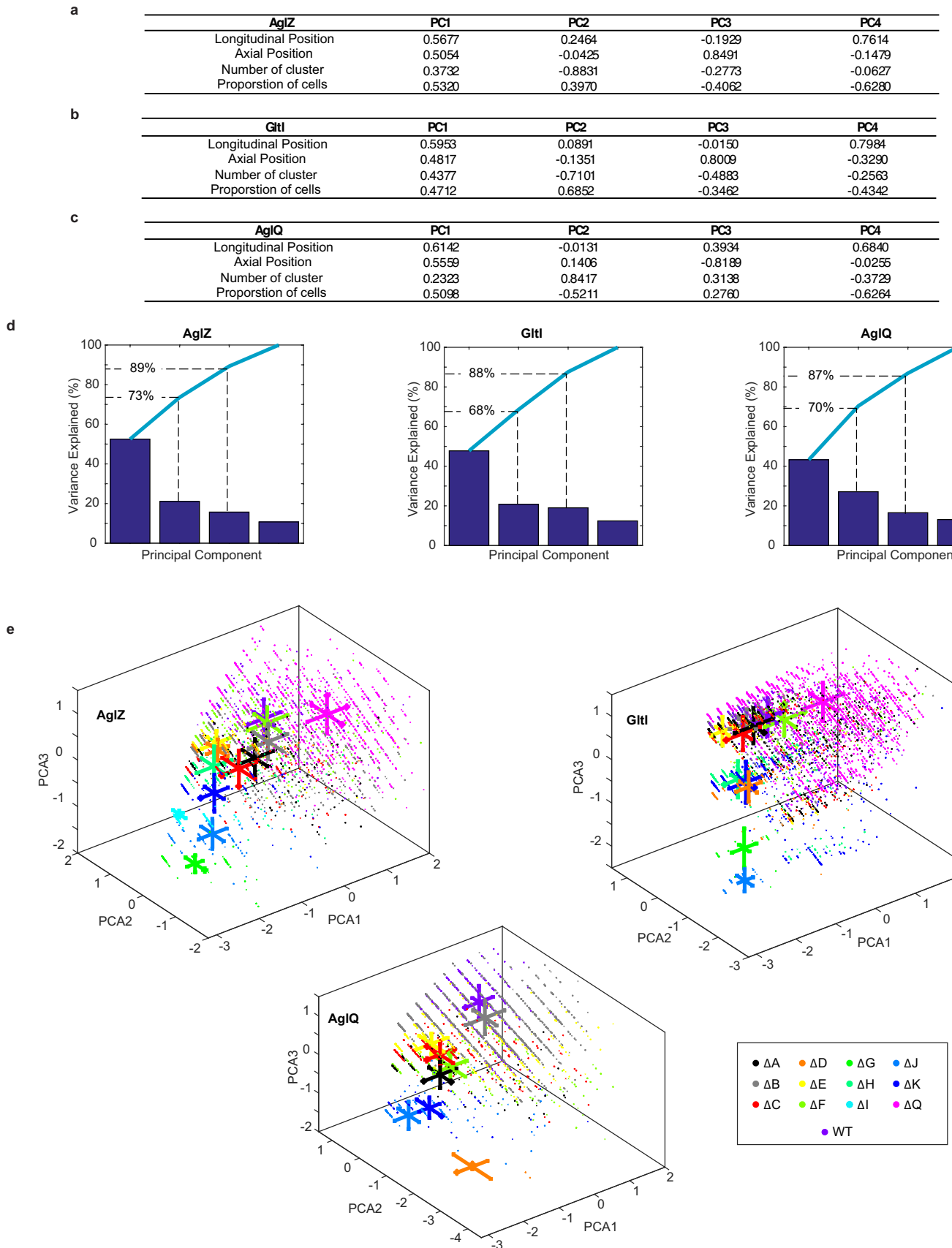
projection of the 2D images on the model 3D cell cylinder (left, β angle) is plotted against the linear displacement of the cell. Each TADA cluster moved at the same radial speed and proportionally to the speed of the cell, indicating that TADA clusters are inert objects reporting on the rigid-body movement of the cell. **f**, Three dimensional trajectories of TADA-bright clusters reconstructed by astigmatism. In the absence of astigmatism, the size of TADA clusters corresponds to the diffraction limit of light, and they are circular (that is, the size of the PSF is the same in perpendicular directions), making the astigmatic analysis of axial position possible. **g**, TADA-bright clusters rotate clockwise. Cluster intensity fluctuations and positions relative to the cell axis are shown over time (left) in a representative cell (right). The black arrow points to the analysed cluster. The representative cell shown in the right panel was isolated from others in the field with a black mask ($n = 10$; three technical replicates).



Extended Data Figure 3 | Analysis of AglZ-YFP, GltI-YFP and AglQ-mCherry in *agl* and *glt* mutant backgrounds. **a**, Each fluorescent functional fusion gene was introduced in place of the wild-type gene in each genetic background shown. Typical examples are shown for each strain. Crossed boxes indicated genetic backgrounds that were not obtained for this study. Scale bar, 2 μ m. **b**, Cluster detection and analysis chart. Phase contrast and fluorescence images were processed so as to respectively extract cell masks of isolated cells (compared edited mask



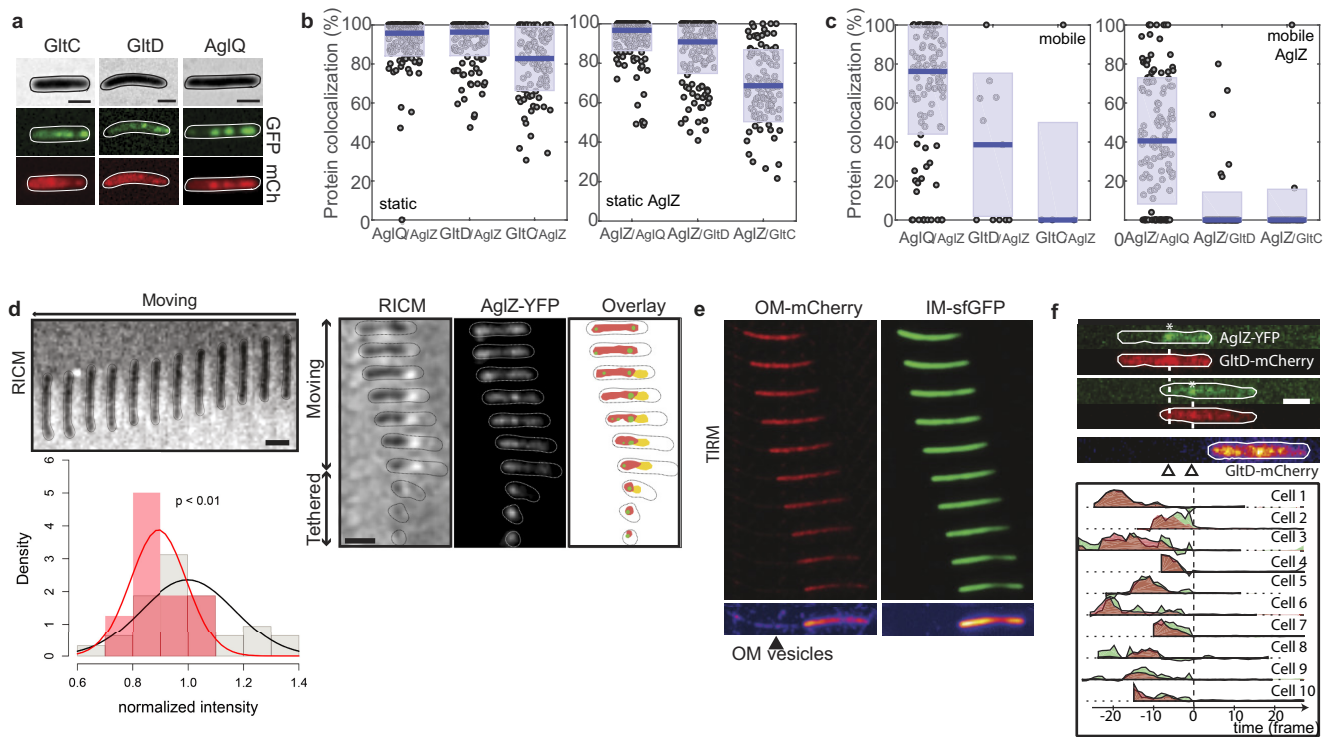
to raw mask) and the position of fluorescence clusters following the application of a fluorescence bandpass filter. Note that the intensity of the fluorescence clusters was not exploited owing to lack of robustness and day-to-day fluctuations. The cluster coordinates were then defined relative to cell coordinates with the Microbe J plugin (<http://www.indiana.edu/~microbej/>) in Fiji, compiled in R sheets and further analysed by PCA using custom-written code in Matlab.



Extended Data Figure 4 | See next page for caption.

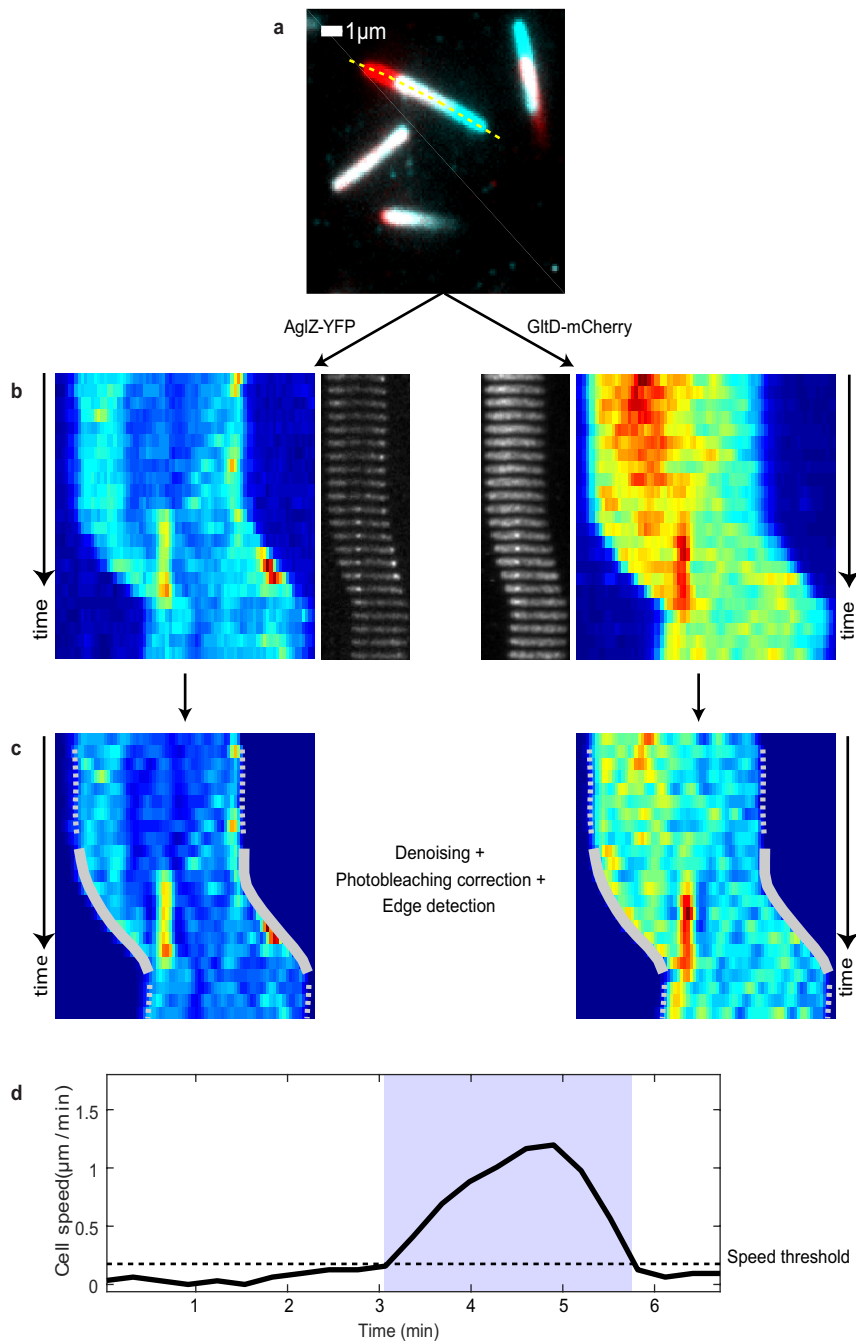
Extended Data Figure 4 | PCA of AglZ–YFP, GltI–YFP and AglQ–mCherry in *agl* and *glt* mutant backgrounds. **a–c**, Coefficients of the principal components (PCs) for AglZ–YFP, GltI–YFP and AglQ–mCherry. PCs are the eigenvectors of the correlation matrix calculated from the four parameters indicated in the first column of the tables. Together, PCs form an orthogonal basis in which the vectors are uncorrelated. PCs are sorted according to the amount of variability in the data they describe, PC1 having the largest effect (that is, variance) and PC4 the least. **d**, Scree plots displaying the variance associated to each PC. The bar plot represents

the variance associated with each PC for a given fusion (from left to right: AglZ–YFP, GltI–YFP and AglQ–mCherry). The cumulative variance is also plotted (light blue line). Note that PC1–2 describe on average 70% of the total variance and PC1–3 more than 87%. **e**, Projection of the data in the space defined by the three first PCs. For each mutant, data are represented by a scatter plot of a specific colour (see inset for colour code). For each direction and each mutant, the average and s.d. of the data are symbolized by a single bold line: the centre of the line represents the average and its length the s.d.



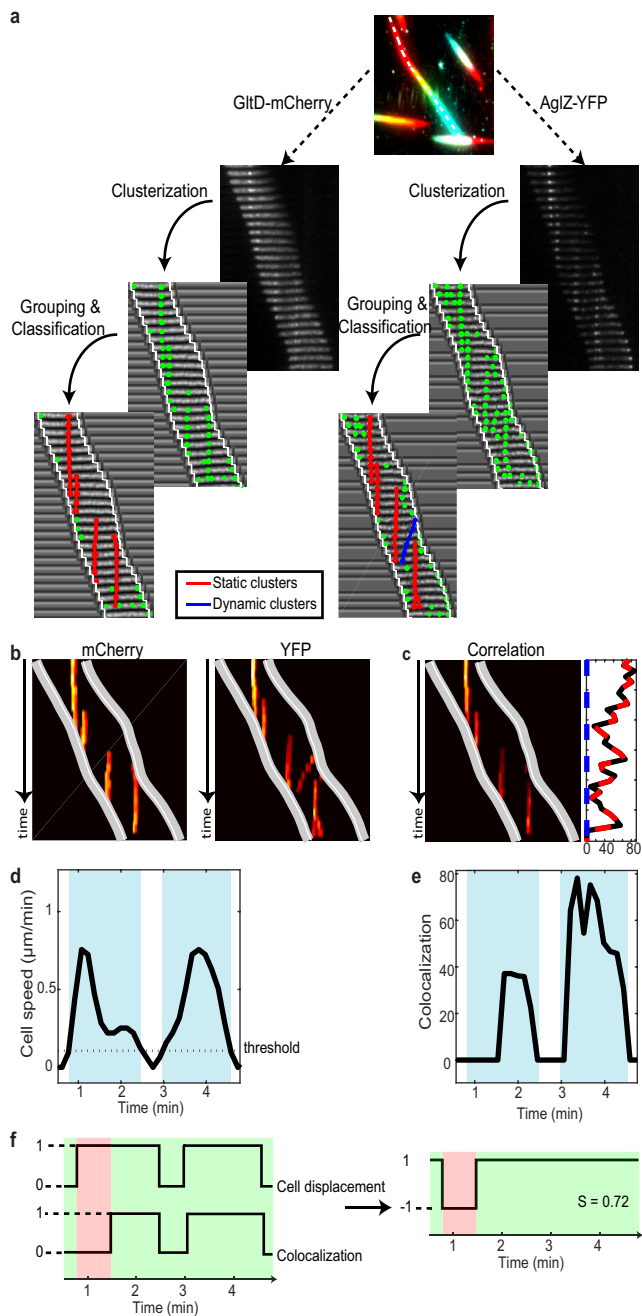
Extended Data Figure 5 | Motility is propelled by cyclic interactions between the inner membrane-localized motor and outer membrane-localized adhesins of the motility complex. **a**, Epifluorescence analysis of representative cells expressing AglZ-YFP-AglQ/GltD/GltC-mCherry. In each case, fluorescent functional fusions are expressed in place of the wild-type gene. Note that while AglZ-YFP and AglQ-mCherry clusters can be detected, GltC-mCherry and GltD-mCherry appear mostly diffuse around the cell envelope with these imaging conditions. Forty cells were imaged for AglZ-YFP-AglQ with two biological replicates; 232 cells were imaged for AglZ-YFP-GltD with three biological replicates; and 55 cells were imaged for AglZ-YFP-GltC with three biological replicates. Scale bar, 2 μ m. **b**, Protein co-localization in static clusters. For each cell analysed, a percentage of co-localization is computed for proteins detected only in static clusters. Values range from 0 when no co-localization between the two proteins was detected in the cell to 100% when the two proteins were always detected together. The left panel shows the percentage of co-localization for AglQ, GltD or GltC with respect to AglZ. Single data are represented by a scatter plot (o), the median co-localization value is symbolized by a blue line and the s.d. by light grey boxes. On average, 96% of AglQ clusters colocalized with AglZ ($n = 153$ clusters; two biological replicates), 96% of GltD ($n = 120$; seven biological replicates) and 83% for GltC ($n = 100$; three biological replicates). Inversely, the right panel represents the percentage of co-localization of AglZ with respect to AglQ (97%, $n = 152$; two biological replicates), GltD (91%, $n = 120$; seven biological replicates) and GltC (69%, $n = 100$; three biological replicates), respectively. **c**, Protein co-localization in mobile clusters. Box-plots read as in **b** and describe the percentage of co-localization for proteins detected only in dynamic clusters. The left panel illustrates the co-localization of AglQ, GltD or GltC with respect to AglZ (76%, $n = 106$, two biological replicates; 39%, $n = 11$, seven biological replicates; and 0%, $n = 4$, three

biological replicates, respectively). The right panel shows the percentage of co-localization of AglZ with respect to AglQ (41%, $n = 125$; two biological replicates), GltD (0%, $n = 72$; seven biological replicates) and GltC (0%, $n = 41$; three biological replicates). From the two panels, it appears that co-localization in dynamic clusters is essentially observed between AglZ and AglQ. For GltD and GltC, dynamic clusters are almost never detected ($n = 11$ for GltD, $n = 4$ for GltC) leading to a co-localization score close or equal to 0%. **d**, AglZ-YFP clusters localize within adhesive contact zones. Left, RICM of a representative gliding cell ($n = 10$, two biological replicates, 30-s time frames; scale bar, 2 μ m) showing intimate connection with the chitosan-coated glass surface (dark zone). Right, adhesions and AglZ-YFP cluster localization in detaching cells by RICM and combined epifluorescence microscopy (time frames, 30 s; scale bar, 2 μ m). The graph represents the distribution of RICM intensities at AglZ-YFP cluster positions (red line) compared to the average intensity along the whole cell body (black line). Data obtained for $n = 20$ cells; two biological replicates. **e**, Gliding *Myxococcus* cells deposit outer membrane vesicles in their wake. TIRFM images of a motile cell expressing both outer membrane sfGFP and inner membrane mCherry. Outer membrane vesicles are deposited, suggesting that the cell is firmly adhered to the underlying surface. Shown is a representative cell ($n = 60$; 12 technical replicates). **f**, GltD-mCherry, a periplasmic Glt protein, is not released by gliding cells at focal adhesion complexes. Top, TIRFM snapshots of a representative cell expressing both GltD-mCherry (red) and AglZ-YFP (green). The position of the GltD clusters on the surface coincides with position of focal adhesion complexes (white asterisk). Time frames, 15 s; scale bar, 2 μ m. Bottom, variation of intensity for GltD-mcherry (red) and AglZ-YFP (green) as a function of time before (negative time) and after (positive time) the cell moved away from the focal adhesion position, shown for $n = 10$ cells (two biological replicates).

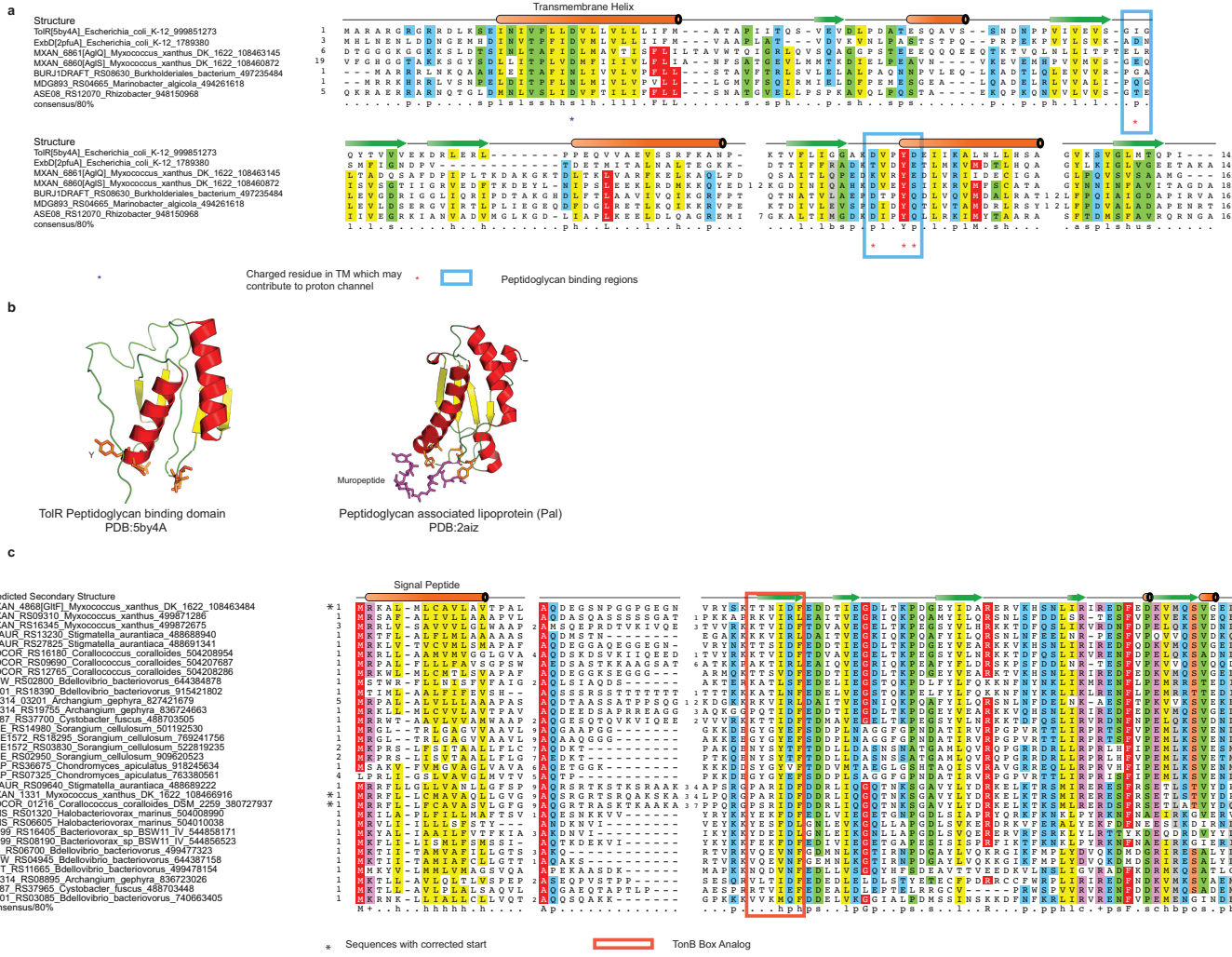

Extended Data Figure 6 | Image analysis for TIRFM experiments.

a, Temporal RGB image computed from fluorescence images (mCherry for this example). Images were summed together and colour coded from blue (first image) to red (last image). Immobile cells appear uniformly white whereas moving cells show coloured extremities. Cell trajectory is represented by a yellow dotted line. **b**, For the two imaging channels (YFP and mCherry), a kymograph and a montage were calculated. Kymograph reads from top (first image) to bottom (last image), each line representing the average fluorescent intensity computed along the cell trajectory. The montage shows for each acquisition an image of the cell after applying a

straightening algorithm. Clusters of proteins (AglZ-YFP or AglQ/GltD/GltI-mCherry) appear as bright spots at the centre of the cell. **c**, Kymographs after applying a denoising algorithm. The cell outline was depicted either by a dotted white line when the cell was immobile or by a continuous white line when the cell was gliding on the surface. **d**, Cell speed as a function of acquisition time. For each cell, a threshold was defined that depended on the SNR and the sample lateral stability during TIRFM acquisition. When the cell speed was below this threshold (horizontal dotted line), the cell was considered immobile. Phases associated with cell movement are highlighted in blue.



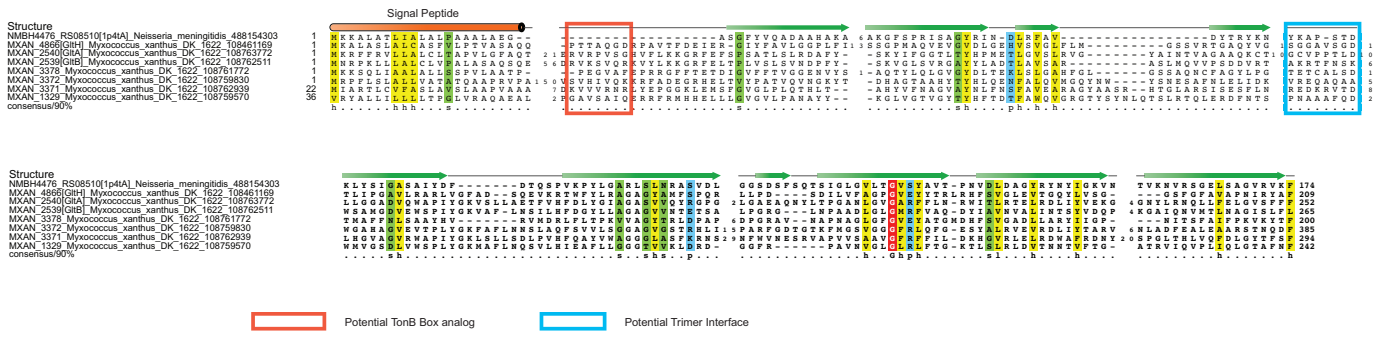
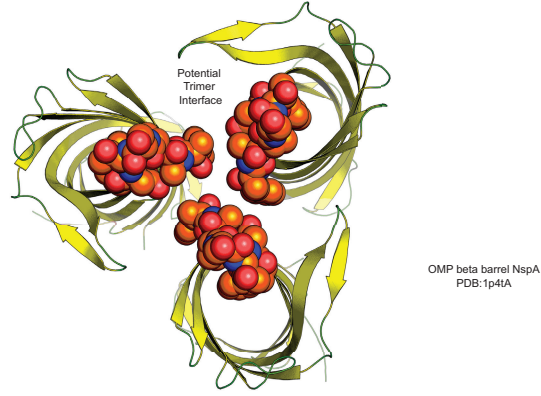
Extended Data Figure 7 | Co-localization estimation and correlation with cell movement. **a**, Co-localization between YFP-tagged and mCherry-tagged proteins was calculated in three steps. For each channel (YFP and mCherry), a threshold was applied to the montage in order to detect protein clusters (clusterization). When the same cluster was observed in successive images, its localizations were stitched together manually and finally classified as either static (red) or dynamic/mobile (blue). **b**, For each channel, a protein-detection map was computed from the kymograph and the positions of the detected clusters. The cell outline was depicted by two white lines. **c**, The co-localization map was obtained by multiplying the two protein-detection maps. In the inset, the cumulative intensities associated with static (red) and dynamic (blue) clusters are plotted as a function of time. **d**, Cell speed as a function of acquisition time. Blue boxes represent regions in which cell speed is higher than the threshold. **e**, Cumulative co-localization intensity (static and dynamic) as a function of acquisition time. Blue boxes represent regions with high cell speeds. **f**, Curves from **d** and **e** were binarized. For the cell speed, the value was set to '0' when the speed was below the threshold (immobile cell) and to '1' when it was above (gliding cell) (left). For the co-localization, the value was set to '1' when co-localization was detected, '0' otherwise (left). A correlation curve (right) was then computed by comparing the two curves. At each time-point, if the values of the two binarized curves were equal (1/1 or 0/0, green highlighted areas), the correlation was set to '1'. Otherwise, it was set to '-1' (red highlighted area). Finally, the correlation score was defined as the average of all the correlation values.



Extended Data Figure 8 | Bioinformatics analysis of AglQ/S and GltF.

a, AglQ and AglS carry a potential peptidoglycan (PG)-binding site. Multiple alignment of AglQ, AglS and their paralogues with TolR(5by4A) and ExbD(2pfuA). The gene name, organism name and GI (NCBI) accession number are given. The structure is shown on top and the 80% consensus is shown below the alignment. **b**, Cartoon views of the structures are shown below with the residues known or predicted to bind peptidoglycan shown as sticks. **c**, The GltF family of proteins found in delta-proteobacteria. Multiple alignment of the GltF family is shown and

labelled using gene name, organism name and GI. The potential TonB box analogue is indicated. The TonB box can be most generally defined as an extended region that forms a β -strand-like structure that is not paired with other β -strands into a structural unit. The TonB box typically has two polar residues, T/S, and classically an acidic/amide residue. The GltF sequence profile analysis shows that GltF is related to the N-terminal region of certain OMP barrels that do contain a potential TonB-box like peptide.

a**b**

Extended Data Figure 9 | Bioinformatics analysis of the GltA/B/H system. **a**, Multiple alignment of the β -barrel OMP proteins GltA, GltB and GltH and their paralogues with NspA (1p4tA). Note the presence of TonB box analogues in GltA and GltB but not GltH. **b**, Cartoon view of the inferred trimer of β -barrels based on the NspA structure with the residues predicted to form a trimeric interaction interface shown as spheres.